Monthly Notices of the ROYAL ASTRONOMICAL SOCIETY

MNRAS **464,** 2378–2395 (2017)
Advance Access publication 2016 September 22

doi:10.1093/mnras/stw2392

CARMA observations of massive *Planck*-discovered cluster candidates at $z \gtrsim 0.5$ associated with *WISE* overdensities: breaking the size–flux degeneracy

C. Rodríguez-González,[1★] R. R. Chary,[1] S. Muchovej,[2] J.-B. Melin,[3] F. Feroz,[4] M. Olamaie[4] and T. Shimwell[5]

[1] *US Planck Data Center, MS220-6, Pasadena, CA 91125, USA,*
[2] *Owens Valley Radio Observatory, California Institute of Technology, Big Pine, CA 93513, USA*
[3] *DSM/Irfu/SPP, CEA-Saclay, F-91191 Gif-sur-Yvette Cedex, France*
[4] *Astrophysics Group, Cavendish Laboratory, JJ Thomson Avenue, Cambridge CB3 0HE, UK*
[5] *Leiden Observatory, Leiden University, NL-2300 RA Leiden, the Netherlands*

Accepted 2016 September 21. Received 2016 August 18; in original form 2014 July 27

ABSTRACT

We use a Bayesian software package to analyse CARMA-8 data towards 19 unconfirmed *Planck* Sunyaev–Zel'dovich-cluster candidates from Rodríguez-González et al. that are associated with significant overdensities in *WISE*. We use two cluster parameterizations, one based on a (fixed shape) generalized-NFW (gNFW) pressure profile and another on a β gas density profile (with varying shape parameters) to obtain parameter estimates from the CARMA-8 data for the nine CARMA-8-detected clusters. Results from the β model show that our cluster candidates exhibit a heterogeneous set of brightness–temperature profiles. Comparison of *Planck* and CARMA-8 measurements show good agreement in Y_{500} and an absence of obvious biases. Applying a *Planck* prior in Y_{500} to the CARMA-8 gNFW results reduces uncertainties in Y_{500} and Θ_{500} dramatically (by a factor >4), relative to the independent *Planck* or CARMA-8 measurements. From this combined analysis, we find that our sample is comprised of massive (Y_{500} ranging from $3.3^{+0.2}_{-0.2}$ to $10^{+1.1}_{-1.5} \times 10^{-4}$ arcmin^2, sd $= 2.2 \times 10^{-4}$), relatively compact (θ_{500} ranging from $2.1^{+0.1}_{-0.3}$ to $5.5^{+0.2}_{-0.8}$ arcmin, sd $= 1.0$) systems. Spectroscopic Keck/MOSFIRE data confirmed a galaxy member of one of our cluster candidates at $z = 0.565$. At the preferred photometric redshift of 0.5, we estimate the cluster mass $M_{500} \approx 0.8 \pm 0.2 \times 10^{15}\,\mathrm{M}_{\odot}$. We here demonstrate a powerful technique to find massive clusters at intermediate ($z \gtrsim 0.5$) redshifts using a cross-correlation between *Planck* and *WISE* data, with high-resolution CARMA-8 follow-up. We also use the combined capabilities of *Planck* and CARMA-8 to obtain a dramatic reduction, by a factor of several, in parameter uncertainties.

Key words: cosmology: observations – large-scale structure of Universe – infrared: galaxies – radio continuum: general.

1 INTRODUCTION

The *Planck* satellite (Tauber et al. 2010; Planck Collaboration I 2011a) is a third-generation space-based mission to study the cosmic microwave background (CMB) and its foregrounds. It has mapped the entire sky at nine frequencies from 30 to 857 GHz, with an angular resolution of 33–5 arcmin, respectively. Massive clusters have been detected in the *Planck* data via the Sunyaev–Zel'dovich (SZ) effect (Sunyaev & Zel'dovich 1972). *Planck* has published a cluster catalogue containing 1227 entries, out of which 861 are confirmed associations with clusters. 178 of these were previously unknown clusters, while a further 366 remain unconfirmed (Planck Collaboration XXIX 2014b). The number of cluster candidates identified in the second data release, PR2, has now reached 1653. The cluster counts are being used to measure the cluster mass function and constrain cosmological parameters (Planck Collaboration XX 2013a). However, using cluster counts to constrain cosmology relies, amongst other things, on understanding the completeness of the survey and measuring both the cluster masses and redshifts accurately (for a comprehensive review, see, e.g. Voit 2005; Allen, Evrard & Mantz 2011). To do so, it is crucial to identify sources of bias and to minimize uncertainty in the translation from cluster observable to mass. Regarding cluster mass, since it is not a direct observable, the best mass-observable relations need to be characterized in order to translate the *Planck* SZ signal into a cluster mass.

★ E-mail: carmen.rodrig25@gmail.com

Table 1. Details of the sample of *Planck*-detected cluster candidates analysed in this work and their CARMA-8 observations; for additional information, the reader is strongly encouraged to look at Paper I. For simplicity and homogeneity in the cluster-naming convention, we use a shorthand ID for the targets. The PSZ (Union catalogue) name (Planck Collaboration XXIX 2014b) is provided, where available†. The right ascension (RA) and declination (Dec.) coordinates (J2000) correspond to the map centre of our observations while the cluster coordinates are in Table 4. For the short and long baseline data, we provided the visibility noise. Targets that have been detected in the CARMA-8 data have their ID highlighted. The SZ decrement towards P014 had a low signal-to-noise ratio (SNR) (4.2) and the SZ signal in the CARMA-8 imaged data was considered tentative in Paper I.

Cluster ID	Union name	RA ($^{\mathrm{h\,m\,s}}$)	Dec. ($^{\circ}\,'\,''$)	Short baseline (0–2 kλ) σ (mJy beam^{-1})^{a}	Long baseline (2–8 kλ) σ (mJy beam^{-1})^{a}
P014	PSZ1G014.13+38.38	16 03 21.62	03 19 12.00	0.309	0.324
P028	PSZ1G028.66+50.16	15 40 10.15	17 54 25.14	0.433	0.451
P031	–	15 27 37.83	20 40 44.28	0.727	0.633
P049	–	14 44 21.61	31 14 59.88	0.557	0.572
P052	–	21 19 02.42	00 33 00.00	0.368	0.386
P057	PSZ1G057.71+51.56	15 48 34.13	36 07 53.86	0.451	0.482
P086	PSZ1G086.93+53.18	15 13 53.36	52 46 41.56	0.622	0.599
P090	PSZ1G090.82+44.13	16 03 43.65	59 11 59.61	0.389	0.427
P097	–	14 55 13.99	58 51 42.44	0.653	0.660
P109	PSZ1G109.88+27.94	18 23 00.19	78 21 52.19	0.562	0.517
P121	PSZ1G121.15+49.64	13 03 26.20	67 25 46.70	0.824	0.681
P134	PSZ1G134.59+53.41	11 51 21.62	62 21 00.18	0.590	0.592
P138	PSZ1G138.11+42.03	10 27 59.07	70 35 19.51	2.170	0.982
P170	PSZ1G171.01+39.44	08 51 05.10	48 30 18.14	0.422	0.469
P187	PSZ1G187.53+21.92	07 32 18.01	31 38 39.03	0.411	0.412
P190	PSZ1G190.68+66.46	11 06 04.09	33 33 45.23	0.450	0.356
P205	PSZ1G205.85+73.77	11 38 13.47	27 55 05.62	0.385	0.431
P264	–	10 44 48.19	−17 31 53.90	0.476	0.513
P351	–	15 04 04.90	−06 07 15.25	0.355	0.392

Notes. †Since the cluster selection criteria, as well as the data for the cluster extraction, are different to those for the PSZ catalogue, not all the clusters in this work have an official *Planck* ID.
[a]Achieved rms noise in corresponding maps.

The accuracy of the *Planck* measurements of the integrated SZ effect at intermediate redshifts where, e.g. X-ray data commonly reach out to, is limited by its resolution (≈10 arcmin at SZ-relevant frequencies) because the integrated SZ signal exhibits a well-known degeneracy with the cluster angular extent (see e.g. Planck Collaboration XXIX 2014b). Higher resolution SZ follow-up of *Planck*-detected clusters can help constrain the cluster size by measuring the spatial profile of the temperature decrement and identify sources of bias. Moreover, a recent comparison of the integrated SZ signal measured by the Arcminute MicroKelvin Imager (AMI; Zwart et al. 2008) on arcminute scales and by *Planck* showed that the *Planck* measurements were systematically higher by ≈35 per cent (Planck Collaboration II 2013a). This study, and its follow-up paper on 99 clusters (Perrott et al. 2015), together with another one by Muchovej et al. (2012) comparing data from the eight-element Combined Array for Research in Millimeter-wave Astronomy (CARMA-8) interferometer and the *Planck* Satellite towards two systems have demonstrated that cluster parameter uncertainties can be greatly reduced by combining both data sets.

In this work, we have used CARMA-8 (see Muchovej et al. 2007 for further details) to undertake high-spatial resolution follow-up observations at 31 GHz towards 19 unconfirmed *Planck* cluster candidates[1] (Table 1). Our primary goal was to attempt to identify massive clusters at high redshifts. For this reason, our candidate clusters were those *Planck* SZ-candidates that had significant overdensities of galaxies in the *WISE* early data release (Wright et al. 2010) ($\gtrsim$1 galaxy arcmin^{-2}) and a red object[2] within 2.5 arcmin fainter than 15.8 Vega mag in the *WISE* 3.4-micron band (an $\sim L_*$ galaxy with stellar mass of 10^{11} M$_\odot$ at $z \approx 1$ is about 15.5 Vega mag), to maximize the chances of choosing $z > 1$ systems. Similar work using *WISE* to find distant clusters has been undertaken by the Massive and Distant Clusters of *WISE* Survey, which, in Gettings et al. (2012), confirmed their first $z \approx 1$ cluster.

This work is presented as a series of two articles. The first one, Rodríguez-Gonzálvez et al. (2015, hereafter Paper I), focused on the sample selection, data reduction, validation using ancillary data and photometric-redshift estimation. This second paper is organized as follows. In Section 2, we describe the cluster parameterizations for the analysis of the CARMA-8 data and present cluster parameter constraints for each model. In addition, we include Bayesian evidence values between a model with a cluster signal and a model without a cluster signal to assess the quality of the detection

[1] The *Planck* SZ catalogue used for the initial selection was an intermediate *Planck* data product known internally as DX7. *Planck* data are collected and reduced in blocks of time. The DX7 maps used in this analysis correspond to the reduction of *Planck* data collected from 2009 August 12 to 2010 November 28, which is the equivalent to 3 full all-sky surveys, using the v4.1 processing pipeline. The DX7 maps used in this work are part of an internal release amongst the Planck Collaboration members and, thus, is not a publicly available data product. It should be noted that the public DR1 PSZ catalogue supersedes the preliminary DX7 catalogue used for our selection.

[2] We describe as red the objects whose [3.4]–[4.6] *WISE* colours are > -0.1 (in AB mag, 0.5 in Vega). This is known as the mid-infrared criterion and has been shown by e.g. Papovich (2008) to preferentially select $z > 1$ objects.

and identify systems likely to be spurious. *Planck*-derived cluster parameters and estimates of the amount of radio-source contamination to the *Planck* signal are given in Section 3. Improved constraints in the Y_{500}–θ_{500} plane from the application of a *Planck* prior on Y_{500} to the CARMA-8 results are provided in Section 4. In Section 5, we discuss the contamination of *Planck* SZ fluxes by nearby radio sources. In Section 6, we discuss the properties of the ensemble of cluster candidates, including their location, morphology and cluster-mass estimates and present spectroscopic confirmation for one of our targets. In this section, we also compare the *Planck* and CARMA-8 data and show how our results relate to similar studies. We note that for homogeneity, since not all the cluster candidates in this work are included in the PSZ (Union catalogue; Planck Collaboration 2013 XXIX), we assign a shorthand cluster ID to each system (see Table 1).

Throughout this work, we use J2000 coordinates, as well as a Λcold dark matter cosmology with $\Omega_{\rm m} = 0.3$, $\Omega_\Lambda = 0.7$, $\Omega_{\rm k} = 0$, $\Omega_{\rm b} = 0.041$, $w_o = -1$, $w_{\rm a} = 0$ and $\sigma_8 = 0.8$. H_0 is taken as 70 km s^{-1} Mpc^{-1}.

2 QUANTITATIVE ANALYSIS OF CARMA-8 DATA

2.1 Parameter estimation using interferometric data

In this work we have used McAdam, a Bayesian analysis package, for the quantitative analysis of the cluster parameters. This package has been used extensively to analyse cluster signals in interferometric data from AMI (see e.g. AMI Consortium: Rodríguez-Gonzálvez et al. 2012; AMI Consortium: Shimwell et al. 2013b; Schammel et al. 2012 for real data and AMI Consortium: Olamaie et al. 2012 for simulated data; in Section 6.5, we compare the AMI results on *Planck* clusters in more detail) and once before on CARMA-8 data (AMI Consortium: Shimwell et al. 2013a). McAdam was originally developed by Marshall, Hobson & Slosar (2003) and later adapted by Feroz et al. (2009) to work on interferometric SZ data using an inference engine, MULTINEST (Feroz & Hobson 2008; Feroz, Hobson & Bridges 2008), that has been optimized to sample efficiently from complex, degenerate, multipeaked posterior distributions. McAdam allows for the cluster parameters and radio source/s (where present) to be fitted simultaneously directly to the short baseline (SB; ∼0.4–2 kλ) *uv* data in the presence of receiver noise and primary CMB anisotropies. The high-resolution, long baseline (LB; ∼2–10 kλ) data are used to constrain the flux and position of detected radio sources; these source-parameter estimates are then set as priors in the analysis of the SB data (see Section 2.2.3). Our short integration times required all of the LB data to be used for the determination of radio-source priors and none of the LB data were included in the McAdam analysis of the SB data. Undertaking the analysis in the Fourier plane avoids the complications associated with going from the sampled visibility plane to the image plane. In McAdam, predicted visibilities $V_\nu^{\rm p}(\boldsymbol{u}_i)$ at frequency ν and baseline vector $\boldsymbol{u}_i$, are generated and compared to the observed data through the likelihood function (see Feroz et al. 2009 for a detailed overview).

The observed SZ surface brightness towards the cluster electron reservoir can be expressed as

$$\Delta I_{\rm CMB} = \Delta T_{\rm CMB} \left.\frac{{\rm d}B(\nu, T)}{{\rm d}T}\right|_{T_{\rm CMB}}, \quad (1)$$

where $\frac{{\rm d}B(\nu,T)}{{\rm d}T}|_{T_{\rm CMB}}$ is the derivative of the blackbody function at $T_{\rm CMB}$ – the temperature of the CMB radiation (Fixsen et al. 1996). The CMB brightness temperature from the SZ effect is given by

$$\Delta T_{\rm CMB} = f(\nu) y T_{\rm CMB}. \quad (2)$$

Here, $f(\nu)$ is the frequency (ν)-dependent term of the SZ effect,

$$f(\nu) = \left(x\frac{e^x+1}{e^x-1} - 4\right)(1 + \delta_{\rm SZ}(x, T_{\rm e})), \quad (3)$$

where the $\delta_{\rm SZ}$ term accounts for relativistic corrections (see Itoh, Kohyama & Nozawa 1998), $T_{\rm e}$ is the electron temperature, $x = h\nu/{\rm k_B}T_{\rm CMB}$, h is Planck's constant and $\rm k_B$ is the Boltzmann constant. To calculate the contribution of the cluster SZ signal to the (predicted) visibility data, the Comptonization parameter, y, across the sky must be computed:

$$y(s) = \frac{\sigma_{\rm T}}{m_{\rm e}c^2}\int_{-\infty}^{+\infty} n_{\rm e}(r)k_{\rm B}T_{\rm e}(r){\rm d}l \propto \int_{-\infty}^{+\infty} P_{\rm e}(r){\rm d}l. \quad (4)$$

Here, $\sigma_{\rm T}$ is the Thomson scattering cross-section, $m_{\rm e}$ is the electron mass, $n_{\rm e}(r)$, $T_{\rm e}(r)$ and $P_{\rm e}(r)$ are the electron density, temperature and pressure at radius r, respectively, c is the speed of light and dl is the line element along the line of sight. The projected distance from the cluster centre to the sky is denoted by s, such that $r^2 = s^2 + l^2$. The integral of y over the solid angle $d\Omega$ subtended by the cluster is proportional to the volume-integrated gas pressure, meaning that this quantity correlates well with the mass of the cluster. For a spherical geometry, this is given by

$$Y_{\rm sph}(r) = \frac{\sigma_{\rm T}}{m_{\rm e}c^2}\int_0^r P_{\rm e}(r')4\pi r'^2{\rm d}r'. \quad (5)$$

When $r \to \infty$, equation (5) can be solved analytically, as shown in Perrott et al. (2015), yielding the total integrated Compton-y parameter, $Y_{\rm T,\,phys}$, which is related to the SZ surface brightness integrated over the cluster's extent on the sky through the angular diameter distance to the cluster ($D_{\rm A}$) as $Y_{\rm T} = Y_{\rm T,phys}/D_{\rm A}^2$.

2.2 Models and parameter estimates

Analyses of X-ray or SZ data of the intracluster medium (ICM) that aim to estimate cluster parameters are usually based on a parametrized cluster model. Cluster models necessarily assume a geometry for the SZ signal, typically spherical, and functional forms of two linearly-independent thermodynamic cluster quantities such as electron temperature and density. These models commonly make assumptions, such as the cluster gas is in hydrostatic equilibrium or that the temperature or gas fraction throughout the cluster is constant. Consequently, the accuracy and validity of the results will depend on how well the chosen parametrization fits the data and on the effects of the model assumptions (see e.g. Plagge et al. 2010; AMI Consortium: Rodríguez-Gonzálvez et al. 2011; Mroczkowski 2011 for studies exploring model effects in analyses of real data and AMI Consortium: Olamaie et al. 2012; Olamaie, Hobson & Grainge 2013 for similar work on simulated data). In this work, we present cluster parameters calculated from two different models; one is based on a fixed-profile-shape generalized-NFW (gNFW) parametrization, for which typical marginalized parameter distributions for similar interferometric data from AMI have been shown in e.g. Perrott et al. (2015), and a second is based on the β profile with variable shape parameters, where typical marginalized parameter distributions for comparable AMI data have been presented in AMI Consortium: Rodríguez-Gonzálvez et al. (2012). Comparison of marginalized posteriors for CARMA and AMI data in AMI Consortium: Shimwell et al. (2013a) for the β model showed the distributions to be very similar. The clusters presented here are at modest redshifts and are unlikely to be in hydrostatic equilibrium – adopting two models at least allows the dependence of the cluster parameters on the adopted model to be illustrated and a comparison with previous work to be undertaken.

2.2.1 *Cluster model I: observational gNFW parametrization*

For cluster model I, we have used a gNFW (Navarro, Frenk & White 1996) pressure profile in the same fashion as in the analysis of *Planck* data (Planck Collaboration VIII 2011b) to facilitate comparison of cluster parameters. A gNFW pressure profile with a fixed set of parameters is believed to be a reasonable choice since (1) numerical simulations show low scatter amongst cluster pressure profiles, with the pressure being one of the cluster parameters that suffers least from the effects of non-gravitational processes in the ICM out to the cluster outskirts and (2) the dark matter potential plays the dominant role in defining the distribution of the gas pressure, yielding an (pure) NFW form to the profile, which can be modified into a gNFW form to account for the effects of ICM processes (see e.g. Vikhlinin et al. 2005; Nagai, Kravtsov & Vikhlinin 2007b). Using a fixed gNFW profile for cluster models has become a regular practice (e.g. Atrio-Barandela et al. 2008 for *WMAP*, Mroczkowski et al. 2009 for the Sunyaev Zel'dovich Array, Czakon et al. 2015 for BOLOCAM and Plagge et al. 2010 for South Pole Telescope data).

Assuming a spherical cluster geometry, the form of the gNFW pressure profile is the following:

$$P_{\rm e}(r) = P_0 \left(\frac{r}{r_{\rm s}}\right)^{-c} \left[1 + \left(\frac{r}{r_{\rm s}}\right)^{a}\right]^{(c-b)/a}, \qquad (6)$$

where P_0 is the normalization coefficient of the pressure profile and $r_{\rm s}$ is the scale radius, typically expressed in terms of the concentration parameter $c_{500} = r_{500}/r_s$. Parameters with a numerical subscript 500, like c_{500}, refer to the value of that variable within r_{500} – the radius at which the mean density is 500 times the critical density at the cluster redshift. The shape of the profile at intermediate regions ($r \approx r_{\rm s}$), around the cluster outskirts ($r >> r_{\rm s}$) and in the core regions ($r << r_{\rm s}$) is governed by three parameters a, b, c, respectively. Together with c_{500}, they constitute the set of gNFW parameters. Two main sets of gNFW parameters have been derived from studies of X-ray observations (inner cluster regions) and simulations (cluster outskirts) (Nagai et al. 2007b; Arnaud et al. 2010). For ease of comparison with the *Planck* results, as well as with SZ-interferometer data, e.g. from AMI in Planck Collaboration II (2013a), we have chosen to use the gNFW parameters derived by Arnaud et al.: $(c_{500}, a, b, c) = (1.156, 1.0620, 5.4807, 0.3292)$.[3]

In our gNFW analysis, we characterize the cluster by the following set of sampling parameters (Table 2):

$$\mathcal{P}_{\rm c} = (\Delta x_{\rm c}, \Delta y_{\rm c}, \eta, \Phi, \theta_{\rm s} = r_{\rm s}/D_{\rm A}, Y_{\rm T}).$$

Here, $\Delta x_{\rm c}$, $\Delta y_{\rm c}$ are the displacement of the cluster decrement from the pointing centre, where the cluster right ascension is equal to the map centre (provided in Table 1), η is the ellipticity parameter, that is, the ratio of the semiminor and semimajor axes and Φ is the position angle of the semimajor axis, measured N through E, i.e. anticlockwise. We note that the projected cluster decrement is modelled as an ellipse and hence our model is not properly triaxial.

Table 2. Summary of the cluster priors used in our analysis for the observational gNFW cluster parametrization (model I, Section 2.2.1). $\Delta x_{\rm c}$ and $\Delta y_{\rm c}$ are the displacement from the map centre to the centroid of the SZ decrement in RA and Dec., respectively. η is the ellipticity parameter and Φ the position angle. $\theta_{\rm s} = r_{\rm s}/D_{\rm A}$, where $r_{\rm s}$ is the scale radius and $D_{\rm A}$ is the angular size distance to the cluster. $Y_{\rm T}$ is the SZ surface brightness integrated over the cluster's extent on the sky. The $\theta_{\rm s}$ and $Y_{\rm T}$ priors have been previously used in e.g. Planck Collaboration VIII (2011b) and Planck Collaboration II (2013a). These priors were defined in Carvalho et al. (2012) based on realistic simulations of a population of clusters using the Jenkins mass function (Jenkins et al. 2001)) and standard *WMAP* best-fitting cold dark matter cosmology (Hinshaw et al. 2009). We note that the lower limit for the prior on $Y_{\rm T}$ is considerably lower ($\approx$ a factor of 3) than the smallest reported $Y_{\rm T}$ values for clusters detected in the Planck survey e.g. (Planck Collaboration VIII 2011b).

Parameter	Prior
$\Delta x_{\rm c}$	Gaussian centred at pointing centre, $\sigma = 60$ arcsec
$\Delta y_{\rm c}$	Gaussian centred at pointing centre, $\sigma = 60$ arcsec
η	Uniform from 0.5 to 1.0
Φ	Uniform from 0° to 180°
θ_s	$\lambda e^{-\lambda\theta_s}$ with $\lambda = 0.2$ for
	1.3 arcmin $< \theta_{\rm s} <$ 45 arcmin and 0 outside this range
$Y_{\rm T}$	$Y_{\rm T}^{-\alpha}$ for 0.0005 to 0.2 arcmin^2
	and 0 outside this range with $\alpha = 1.6$

The priors used in this analysis are given in Table 2; they have been used previously for the blind detection of clusters in *Planck* data (Planck Collaboration VIII 2011b) and to characterize confirmed and candidate clusters in Planck Collaboration II (2013a). Cluster parameter estimates and the CARMA best-fitting positions derived from model I are provided in Tables 3 and 4, respectively. We include the 2D marginalized posterior distributions for the cluster sampling parameters for one of our clusters, P190, to represent the typical parameter degeneracies seen in our gNFW analysis. The degeneracies shown in Fig. 1 are in line with those seen in similar SZ experiments (see e.g. AMI Consortium: Rodríguez-Gonzálvez et al. 2012). Clearly, some parameters such as the cluster centroid, $Y_{\rm T}$ and $\theta_{\rm s}$ are better constrained than others, like η and ϕ, as a result of our limited resolution and signal-to-noise ratio (SNR). We note that our approach to factor in all sources of uncertainty by, e.g. including the cluster geometry in our sampling parameters, instead of assuming sphericity, like many other studies, does lead to larger uncertainties in the cluster parameters in Table 3. However, we advocate that our implementation provides more realistic uncertainties and parameters like η should be included in the analysis regardless of them having poorer constraints.

2.2.2 *Quantifying the significance of the CARMA-8 SZ detection or lack thereof*

Bayesian inference provides a quantitative way of ranking model fits to a data set. Although the term model technically refers to a position in parameter space $\mathbf{\Theta}$, here we refer to two model *classes*: a model class that allows for a cluster signal to be fit to the data, M_1, and another, M_0, that does not. The parametrization we have used for this analysis has been the gNFW-based model, model I: for the M_1 case, model I was run as described in Section 2.2.1 and for the M_0 case, it was run in the same fashion except for the prior on Y_{500}, which was set to 0, such that no SZ (cluster) signal is included

[3] We note that the Planck Collaboration have also published a new set of gNFW parameters using SZ-based pressure profiles towards 62 nearby massive clusters by utilizing the all-sky coverage and broad frequency of the *Planck* satellite (Planck Collaboration V 2013b).

Table 3. Mean and 68 per cent-confidence uncertainties for McAdam-derived cluster parameters when fitting for an observational gNFW cluster parametrization (model I; Section 2.2.1) for clusters with a significant SZ detection in the CARMA-8 data (Table 5). The cluster ID is a shorthand naming convention adopted here and in Paper I, since not all our targets have an identifier in the *Planck* Union catalogue (Planck Collaboration XXIX 2014b). Where available, the Union catalogue names are given in Table 1. The derived sampling parameters for the gNFW parametrization are presented in columns 2–7 and their priors are listed in Table 2. Y_{500} is the integrated SZ surface brightness within θ_{500}, where $\theta_{500} = r_{500}/D_{\rm A}$ and $y(0)$ is the central Comptonization parameter, y, equation (4).

Cluster ID	$\Delta x_{\rm c}$ (arcsec)	$\Delta y_{\rm c}$ (arcsec)	Φ (°)	η	$\theta_{\rm s}$ (arcmin)	$Y_{\rm T}$ ($\times 10^{-4}$ arcmin^2)	θ_{500} (arcmin)	Y_{500} ($\times 10^{-4}$ arcmin^2)	$y(0)$ ($\times 10^{-4}$)
P014	25^{+24}_{-23}	-148^{+6}_{-14}	149^{+22}_{-22}	$0.6^{+0.1}_{-0.1}$	4^{+1}_{-1}	20^{+10}_{-11}	$4.3^{+1.2}_{-1.3}$	11^{+5}_{-6}	$1.6^{+0.4}_{-0.4}$
P086	68^{+20}_{-20}	91^{+17}_{-17}	85^{+71}_{-65}	$0.8^{+0.2}_{-0.2}$	3^{+1}_{-2}	20^{+6}_{-15}	$3.7^{+1.6}_{-2.2}$	11^{+3}_{-8}	$2.1^{+0.9}_{-0.8}$
P097	79^{+23}_{-23}	38^{+16}_{-17}	76^{+66}_{-52}	$0.8^{+0.2}_{-0.2}$	3^{+1}_{-1}	11^{+3}_{-6}	$3.2^{+1.2}_{-1.3}$	6^{+2}_{-4}	$1.9^{+0.9}_{-0.8}$
P109	10^{+18}_{-18}	75^{+14}_{-13}	89^{+91}_{-89}	$0.8^{+0.2}_{-0.2}$	3^{+1}_{-1}	10^{+3}_{-5}	$3.1^{+1}_{-1.1}$	6^{+2}_{-3}	$1.9^{+0.8}_{-0.8}$
P170	-59^{+12}_{-12}	10^{+14}_{-14}	69^{+27}_{-26}	$0.7^{+0.2}_{-0.2}$	2^{+1}_{-1}	12^{+3}_{-7}	$2.7^{+0.9}_{-1.2}$	6^{+2}_{-4}	$2.3^{+0.8}_{-0.7}$
P187	64^{+14}_{-14}	-67^{+15}_{-15}	101^{+50}_{-59}	$0.8^{+0.2}_{-0.2}$	4^{+2}_{-2}	23^{+10}_{-18}	$4.1^{+1.8}_{-1.9}$	13^{+5}_{-10}	$1.9^{+0.6}_{-0.6}$
P190	59^{+10}_{-10}	11^{+11}_{-11}	95^{+40}_{-39}	$0.8^{+0.2}_{-0.1}$	3^{+1}_{-1}	16^{+7}_{-11}	$3.5^{+1.4}_{-1.4}$	9^{+4}_{-6}	$2.0^{+0.6}_{-0.6}$
P205	-83^{+11}_{-11}	-26^{+15}_{-15}	79^{+23}_{-23}	$0.7^{+0.2}_{-0.1}$	4^{+2}_{-2}	31^{+13}_{-26}	$4.9^{+2.1}_{-2.2}$	17^{+7}_{-15}	$1.6^{+0.4}_{-0.4}$
P351	-42^{+34}_{-34}	63^{+24}_{-23}	71^{+60}_{-45}	$0.7^{+0.2}_{-0.2}$	5^{+2}_{-2}	19^{+7}_{-14}	$5.3^{+2.3}_{-2.3}$	10^{+4}_{-8}	$0.9^{+0.3}_{-0.4}$

Table 4. Cluster J2000 coordinates derived using the gNFW (model I) fits to the CARMA-8 data.

Cluster ID	RA (h:m:s)	Dec. (d:m:s)
P014	16:03:23.29	03:16:44.00
P086	15:14:00.85	52:48:12.56
P097	14:55:24.17	58:52:20.44
P109	18:23:03.50	78:23:07.19
P170	08:50:59.16	48:30:28.14
P187	07:32:23.03	31:37:32.03
P190	11:06:08.81	33:33:56.23
P205	11:38:07.21	27:54:39.62
P351	15:04:02.09	−06:06:12.24

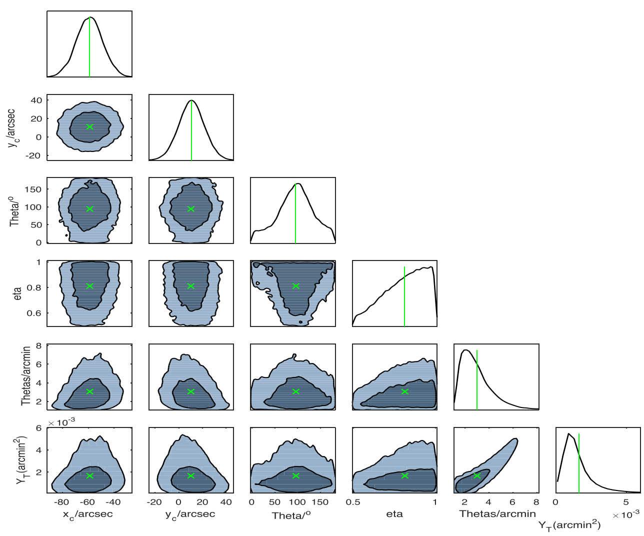

Figure 1. 1D and 2D marginalized distributions for the sampling parameters of our gNFW parametrization for P190. The mean is depicted as a green cross and as a line in the 2D and the 1D plots, respectively.

in the model. Given the data $\boldsymbol{D}$, deciding whether M_1 or M_0 fit the data best can be done by computing the ratio:

$$\frac{\Pr(\mathrm{M}_1|\boldsymbol{D})}{\Pr(\mathrm{M}_0|\boldsymbol{D})} = \frac{\Pr(\boldsymbol{D}|\mathrm{M}_1)}{\Pr(\boldsymbol{D}|\mathrm{M}_0)}\frac{\Pr(\mathrm{M}_1)}{\Pr(\mathrm{M}_0)} = \frac{Z_1}{Z_0}\frac{\Pr(\mathrm{M}_1)}{\Pr(\mathrm{M}_0)}. \tag{7}$$

Here, $K = \frac{\Pr(\boldsymbol{D}|\mathrm{M}_1)}{\Pr(\boldsymbol{D}|\mathrm{M}_0)}$ is known as the Bayes factor and $\frac{\Pr(\mathrm{M}_1)}{\Pr(\mathrm{M}_0)}$ is the prior ratio, that is, the probability ratio of the two model classes, which must be set before any information has been drawn from the data being analysed. Here, we set the prior ratio to unity,[4] i.e. we assume no a priori knowledge regarding which model class is most favourable. The Bayesian evidence Z is calculated as the integral of the likelihood function, $\mathcal{L} = \Pr(\boldsymbol{D}|\boldsymbol{\Theta}, M)$ times the prior probability distribution $\Pi(\boldsymbol{\Theta}) = \Pr(\boldsymbol{\Theta}|M)$,

$$Z = \Pr(\boldsymbol{D}|M) = \int \Pr(\boldsymbol{D}|\boldsymbol{\Theta}, M)\Pr(\boldsymbol{\Theta}|M)\mathrm{d}^{\mathcal{D}}\boldsymbol{\Theta}$$
$$= \int \mathcal{L}(\boldsymbol{\Theta})\Pi(\boldsymbol{\Theta})\mathrm{d}^{\mathcal{D}}\boldsymbol{\Theta}, \tag{8}$$

where $\mathcal{D}$ is the dimensionality of the parameter space. Z represents an average of the likelihood over the prior and will therefore favour models with high-likelihood values throughout the entirety of parameter space. This satisfies Occams razor, which states that the models with compact parameter spaces will have larger evidence values than more complex models, unless the latter fit the data significantly better, i.e. unnecessary complexity in a model will be penalized with a lower evidence value.

The derived Bayes factor is listed in Table 5 along with the corresponding classification of whether or not the cluster was considered to be detected. We find that all the SZ decrements considered to have high SNRs in Paper I have Bayes factors that indicate that the presence of a cluster signature is strongly favoured. However, we do find some tension between the Paper I Modelfit and McAdam results for one of the candidate clusters, P014. In Paper I, this candidate cluster was catalogued as tentative (see appendix B of Paper I for more details). The low SNR[5] of 4.2 for the decrement together with the unusually large displacement from the *Planck* position (≈159 arcsec) suggest this detection is spurious. The lack of an X-ray signature would support this, unless it was a high-redshift cluster or one without a concentrated profile. With regards to the source environment, two sources were detected in the LB data with

[4] Prior ratios need not be set to unity, see e.g. Jenkins & Peacock (2011).

[5] The SNR for the CARMA SZ detections was calculated in Paper I as the ratio of the peak decrement, after correcting for beam attenuation, and the rms of the SB data.

Table 5. Bayes factor, K, for SZ signals detected in the CARMA-8 data by McAdam. Since the prior ratio is set to unity, the Bayes factor provides a measure of the quality of the model fit to the data. For two clusters, P014 and P134, two potential SZ signals were detected in the field of view (FoV) of each observation; the second cluster-like signal is labelled with a 'b'. We adopt Jeffreys (1961) interpretation of K, though with fewer categories, to be even more conservative. We consider $K \leq 0.1$ to be strong evidence against a cluster signal (NC); $0.1 < K \leq 10$ means that our data cannot be used on their own to distinguish robustly between a model with or without a cluster signal (ND) and $K > 10$ indicates there is a strong evidence for the presence of a cluster signal in the data (D). For reference, the signal-to-noise ratio (SNR) for detected clusters (those highlighted in bold font) in CARMA-8 and *Planck* data are given in table 2 of Paper I. As in Table 1, targets that have been detected in the CARMA-8 data have their ID highlighted.

Cluster	Bayes factor	Degree of detection
P014	3.4e+01	D
P014b	4.2e−01	ND
P028	4.6e−01	ND
P031	5.0e−02	NC
P049	2.2e−01	ND
P052	9.5e−01	ND
P057	6.1e−01	ND
P086	3.5e+03	D
P090	1.2e+00	ND
P097	7.9e+02	D
P109	8.4e+02	D
P121	4.9e−01	ND
P134	3.0e−02	NC
P134b	3.0e−04	NC
P170	7.2e+08	D
P187	8.0e+08	D
P190	5.6e+18	D
P205	1.3e+09	D
P264	2.3e+00	ND
P351	2.7e+01	D

a peak 31-GHz flux density of 6.3 and 9.4 mJy, a distance of ≈100 and ≈600 arcsec from the SZ decrement, respectively. The LB data, after subtraction of these radio sources using the Modelfit values, were consistent with noise-like fluctuations, indicating the removal of the radio-source flux worked well. The NRAO VLA Sky Survey (NVSS) results revealed four other radio sources which, due to their location and measured fluxes at 1.4 GHz (as well as their lack of detection in the LB data), are unlikely to contaminate the candidate cluster. The NVSS results also indicate that the radio sources are not extended. The strongest support for the presence of an SZ signature comes from the relatively high *Planck* SNR of 4.5 but this measurement could suffer from the high contamination from interstellar medium emission which mimics itself as the SZ increment at high frequencies and could also result in a large error on its derived position – suggestion of this arises from the strength of the 100 μm emission which is the highest for our sample. Yet, despite these results, the Bayes factor from Table 5 shows that a model with a cluster signature is preferred over the one without. There are potentially quite important differences between the Paper I results and the McAdam evidences, e.g. the Modelfit results are based on an image and single-value fits without simultaneous fits to other parameters, while the McAdam results are derived from fits to the *uv*-plane, taking into account all model parameters, some of which are not strongly constrained by the data. Indeed, we find high scatter in the relation between evidence values and Modelfit-based SNR values but they are positively correlated. Validation of this candidate cluster will require further data. Given the modest significance of the detection of P014 by two different techniques, we decided to include P014 in our McAdam analyses.

Table 6. Summary of the source priors used in our analysis. Values for the position (x_s, y_s) and 31-GHz flux (S_{31}) priors were obtained from the long baseline CARMA-8 data (see Paper I and Section 2.2.3 for further details). The error on the source location is the typical error of the LB data. To account for the fact that the combined cluster and source analysis uses only the short baseline (lower- resolution) data, we model the integrated 31-GHz source flux with a Gaussian, whose width is set to $\sigma = 20$ per cent of the source flux. For the spectral index α_s, we used a wide prior, encompassing reasonable value (see Section 5).

Parameter	Prior
RA$_s$, Dec$_s$	Uniform between ±10 arcsec from the LB-determined position
S_{31}	Gaussian centred at best-fitting Modelfit value with a σ of 20 per cent
α_s	Gaussian centred at 0.6 with $\sigma = 0.5$

2.2.3 *Radio-source model and parameter estimates*

Radio sources are often strong contaminants of the SZ decrement and their contributions must be included in our cluster analysis. In this work, we jointly fit for the cluster, radio source and primary CMB signals in the SB data. The treatment of radio sources is the same for all cluster models. These sources are parametrized by four parameters,

$$\mathbf{\Theta}_s = (\mathrm{RA}_s, \mathrm{Dec}_s, \alpha_s, S_{31}),$$

where RA$_s$ and Dec$_s$ are RA and Dec. of the radio source, α_s is the spectral index, derived from the low fractional CARMA-8 bandwidth and S_{31} is the 31-GHz integrated source flux. We adopt the $S_\nu \propto \nu^{-\alpha_s}$ convention, where S is flux and ν frequency.

The high-resolution LB data were mapped in difmap (Shepherd 1997) to check for the presence of radio sources. Radio-point sources detected in the LB maps were modelled using the difmap task Modelfit. The results from Modelfit were primary beam-corrected using a full width at half-maximum (FWHM) of 660 arcsec by dividing them by the following factor

$$\exp\left(\frac{-r^2}{2\times\sigma^2}\right), \tag{9}$$

where r is the distance of the source to the pointing centre and

$$\sigma = \frac{660}{2\times(2\times\ln(2))^{0.5}}. \tag{10}$$

The primary beam-corrected values were used as priors in the analysis of the SB data (see Table 6). Modelfit values are given in Paper I and McAdam-derived values are provided in Table 7.

2.2.4 *Cluster model II: observational β parametrization*

For this cluster parametrization, we fit for an elliptical cluster geometry, as we did for model I, and model the shape of the SZ

Table 7. Mean and 68 per cent confidence uncertainties for radio-source parameters for sources detected in the LB CARMA-8 data towards candidate *Planck* clusters with a CARMA-8 SZ detection. These parameters have been obtained from the joint cluster + sources fit in McAdam to the SB data using cluster model I (Section 2.2.1).

Source ID	Cluster ID	RA_s ($^{h\,m\,s}$)	σ_{RA_s} (arcsec)	Dec_s ($^{\circ\,\prime\,\prime\prime}$)	σ_{Dec_s} (arcsec)	S_{31} (mJy)	α_s
1	P014	16 03 19.44	3.6	03 16 55.20	3.6	8.1 ± 1.2	0.5 ± 0.4
2	P014	16 03 30.00	3.6	03 26 29.58	3.6	8.9 ± 2.2	0.6 ± 0.4
1	P109	18 22 52.32	7.2	78 23 02.40	7.2	1.8 ± 0.4	0.6 ± 0.5
1	P170	08 51 15.12	7.2	48 37 08.40	7.2	4.6 ± 0.7	0.5 ± 0.5
1	P187	07 32 20.16	3.6	31 41 16.80	3.6	3.7 ± 0.4	0.5 ± 0.5
1	P351	15 04 18.48	7.2	−5 54 50.40	7.2	2.8 ± 0.5	0.6 ± 0.5

Table 8. Summary of the cluster priors used in our analysis for the observational β cluster parametrization (model II, Section 2.2.4). Δx_c and Δy_c are the displacement from the map centre to the centroid of the SZ decrement in RA and Dec., respectively. η is the ellipticity parameter and Φ the position angle. The power-law index β and the core radius r_c are the shape parameters of the density profile and ΔT_0 is the temperature decrement at zero-projected radius.

Parameter	Prior
Δx_c	Gaussian centred at pointing centre, $\sigma = 60$ arcsec
Δy_c	Gaussian centred at pointing centre, $\sigma = 60$ arcsec
η	Uniform from 0.5 to 1.0
Φ	Uniform from 0° to 180°
β	Uniform from 0.4 to 2.5
θ_c	Uniform from 20 to 500 arcsec
ΔT_0	Uniform from −3 to −0.01 mK

temperature decrement with a β-like profile (Cavaliere & Fusco-Femiano 1978):

$$\Delta T_{\rm CMB}(\theta) = \Delta T_0 \left(1 + \left(\frac{\theta}{\theta_c}\right)^2\right)^{(1-3\beta)/2}, \qquad (11)$$

where ΔT_0 is the brightness temperature decrement at zero-projected radius, while β and $r_c = \theta_c \times D_A$ – the power-law index and the core radius – are the shape parameters that give the density profile a flat top at small $\frac{\theta}{\theta_c}$ and a logarithmic slope of 3β at large $\frac{\theta}{\theta_c}$. The sampling parameters for the cluster signal are

$\mathcal{P}_c = (\Delta x_c, \Delta y_c, \eta, \phi, \Delta T_0, \beta, \theta_c)$,

with priors given in Table 8, which allow for the y signal to be computed. Cluster parameter estimates derived from model II are provided in Table 9. We include the 2D marginalized posterior distributions for the cluster sampling parameters for one of our clusters, P190, to represent the typical parameter degeneracies seen in our β analysis, Fig. 2.

It is important to note that, historically, in many SZ analyses, the shape of the β profile has been fixed to values obtained from fits to higher resolution X-ray data. However, these X-ray results primarily probe the inner regions of the cluster and, thus, can provide inadequate best-fitting profile shape parameters for SZ data extending out to larger r. A comparative analysis in Czakon et al. (2015) reveals systematic differences in cluster parameters derived from SZ data using a model-independent method versus X-ray-determined cluster profiles. Several studies have now shown that fits to SZ data reaching r_{500} and beyond preferentially yield larger β values than X-ray data, which tend to yield $\beta = 2/3$ (see e.g. Plagge et al. 2010; AMI Consortium: Hurley-Walker et al. 2012). Using a suitable β (and θ_c) value for the aforementioned typical SZ data can yield results comparable to those of a gNFW profile. In our β parametrization, we allow the shape parameters, β and θ_c, to be fit in McAdam, since they jointly govern the profile shape. While our data cannot constrain either of these variables independently, they can constrain their degeneracy.

Although a large fraction of clusters are well described by the best-fitting gNFW parameterizations, some are not, as can be seen from e.g. the spread in the gNFW parameter sets from fits to individual clusters in the Representative XMM-Newton Cluster Structure Survey (REXCESS) sample (Arnaud et al. 2010). In these cases, modelling the cluster using a fixed (inadequate) set of gNFW

Table 9. Mean and 68 per cent-confidence uncertainties for McAdam-derived cluster parameters when fitting for an observational β cluster parametrization (model II; see Section 2.2.4) for clusters with an SZ detection in the CARMA-8 data (see Table 5). The priors for these sampling parameters are given in Table 8.

Cluster ID	Δx_c (arcsec)	Δy_c (arcsec)	Φ (deg)	η	θ_c ($''$)	β	ΔT_0 (μK)
P014	52^{+6}_{-6}	-137^{+7}_{-9}	90^{+10}_{-10}	$0.7^{+0.3}_{-0.2}$	91^{+14}_{-71}	$1.6^{+0.9}_{-0.9}$	-682^{+145}_{-67}
P086	76^{+15}_{-15}	83^{+15}_{-14}	102^{+78}_{-102}	$0.8^{+0.2}_{-0.3}$	82^{+10}_{-62}	$1.7^{+0.8}_{-1.0}$	-1229^{+415}_{-153}
P097	77^{+8}_{-11}	34^{+6}_{-6}	82^{+98}_{-82}	$0.8^{+0.2}_{-0.3}$	78^{+4}_{-58}	$1.8^{+0.7}_{-1.1}$	-1109^{+505}_{-218}
P109	7^{+5}_{-5}	60^{+5}_{-4}	85^{+21}_{-85}	$0.8^{+0.2}_{-0.3}$	60^{+4}_{-40}	$1.9^{+0.6}_{-0.1}$	-1435^{+357}_{-259}
P170	-58^{+5}_{-6}	4^{+7}_{-7}	63^{+4}_{-11}	$0.7^{+0.3}_{-0.2}$	112^{+23}_{-92}	$1.5^{+1.0}_{-0.8}$	-816^{+231}_{-8}
P187	52^{+6}_{-6}	-48^{+7}_{-6}	92^{+88}_{-92}	$0.8^{+0.2}_{-0.3}$	111^{+20}_{-91}	$1.7^{+0.8}_{-1.0}$	-706^{+172}_{-7}
P190	53^{+4}_{-4}	21^{+5}_{-5}	74^{+106}_{-74}	$0.8^{+0.2}_{-0.3}$	78^{+13}_{-58}	$1.5^{+1.0}_{-0.8}$	-959^{+311}_{-61}
P205	-80^{+6}_{-6}	-19^{+10}_{-11}	74^{+4}_{-7}	$0.6^{+0.1}_{-0.1}$	205^{+39}_{-185}	$1.3^{+1.2}_{-0.6}$	-846^{+304}_{-11}
P351	15^{+20}_{-21}	35^{+18}_{-15}	55^{+10}_{-10}	$0.6^{+0.1}_{-0.1}$	291^{+209}_{-271}	$1.5^{+1.0}_{-0.8}$	-959^{+439}_{-175}

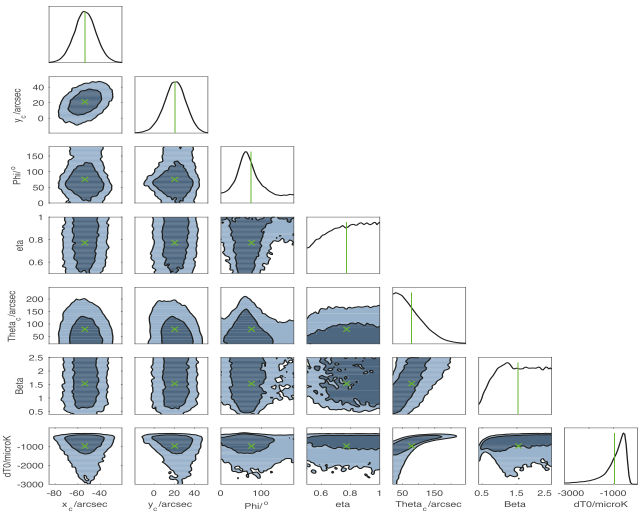

Figure 2. 1D and 2D marginalized distributions for the sampling parameters of our β parametrization for P190. The mean is depicted as a green cross and as a line in the 2D and the 1D plots, respectively.

parameters will return biased, incorrect results, whereas using a β model with varying β and θ_c should provide more reliable results. This is shown in fig. 1 of AMI Consortium: Rodríguez-Gonzálvez et al. (2012) where the data from AMI for a relaxed and a disturbed cluster are analysed with a β parametrization and five gNFW parameterizations, four of which have gNFW sets of parameters drawn from the Arnaud et al. REXCESS sample, three from individual systems and one from the averaged (Universal) profile, and, lastly, one with the average-profile values from an independent study by Nagai et al. (2007b). For both clusters, the Nagai parametrization leads to a larger Y_{500}–θ_{500} degeneracy and larger parameter uncertainties than the Arnaud Universal parametrization. The mean Y_{500} and θ_{500} values obtained from using the β, Universal (Arnaud) and Nagai gNFW profiles were consistent to within the 95 per cent probability contours, but this was not the case for fits using the sets of gNFW parameters obtained from individual fits to REXCESS clusters, indicating that some clusters do not follow a single, averaged profile. Here, comparison of the Bayesian evidence values for β- and gNFW-based analyses showed that the data could not distinguish between them. Our CARMA data for this paper have a similar resolution to the AMI data but, typically, they have much poorer SNRs and similarly cannot determine which of the two profiles provides a better fit to the data. More recently, Sayers et al. (2013b) have derived a new set of gNFW parameters from 45 massive galaxy clusters using BOLOCAM and Mantz et al. (2014) have further shown how the choice of model parameters can have a measurable effect on the estimated Y-parameter.

All sets of gNFW parameters can lead to biases when applied to different sets of data. Given that there is no optimally selected set of gNFW parameters to represent CARMA 31-GHz data towards massive, medium-to-high-redshift clusters ($z \gtrsim 0.5$), we choose to base most of our analysis on the gNFW parameter set from the 'Universal' profile derived by (Arnaud et al. 2010) as this facilitates comparison with the *Planck* analysis and parallel studies between *Planck* and AMI, an interferometer operating at 16 GHz with arcminute resolution.

2.2.4.1 Cluster profiles. Using equation (11) for $\Delta T_{\rm CMB}(\theta)$ (the SZ temperature decrement), and the mean values for ΔT_0, β and θ_c derived from model II fits to the CARMA-8 data (Table 9), in Fig. 3, left, we plot the radial brightness temperature profiles for our sample of CARMA-8-detected candidate clusters. We order them

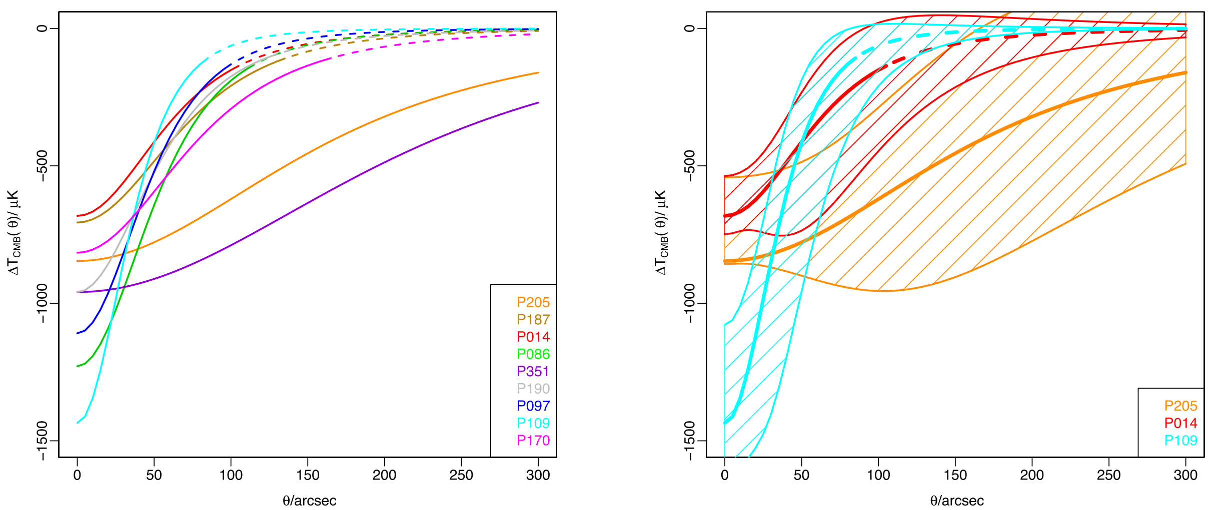

Figure 3. Left: radial brightness temperature profiles derived from equation (11) using the cluster parameter values (ΔT_0, β and θ_c) from fits of model II to the CARMA-8 data (as provided in Table 9). When the profile has dropped to three times the noise in the SB data, the lines turn from solid to dashed. In the legend, the cluster candidates have been ordered by decreasing Y_{500} (Table 3), although it should be noted that for some clusters, the difference in Y_{500} is small. Shallower profiles with the most negative ΔT_0 values and largest θ_{500} values should correspond to the largest Y_{500} from model I. Comparing the volume-integrated brightness temperature profile, $\int T(\theta) 4\pi\theta^2 {\rm d}\theta$ for each cluster from 0 to its θ_{500} (from model I; Table 3) with Y_{500} (model I), shows reasonable correspondence for most systems, with the exception of P351 and P187. Right: best-fitting radial brightness temperature profiles for three clusters, P205, P014 and P109, which span a range of profile shapes (in thick solid lines, same as the corresponding lines in the left panel). However, here we include the upper and lower 68 per cent-confidence limits of each brightness temperature profile in thin solid lines and highlight the region between these limits with diagonal lines. This shows that according to the parameter fits to CARMA-8 data from model II, the clusters in our sample exhibit a heterogenous set of profiles, distinguishable despite the uncertainty. Furthermore, high-resolution SZ data or X-ray data may be insensitive to the large signal from the outer parts of the cluster and introduce an additional uncertainty in the derivation of Y_T, an issue which is addressed through a joint analysis with the *Planck* data.

Table 10. Ratio of the integral of $\int T(\theta)\mathrm{d}\theta$ integrated between 0 and 600 arcsec (≈FWHM of the 100-GHz *Planck* beam) and integrated between 0 and θ_{500} (from Table 3), where the expression for $T(\theta)$ is given in equation (11). This ratio is a measure of concentration of the brightness temperature profile. The most concentrated profile (for P014) is ≈2.5 times more concentrated than the shallowest profile (for P351). Six of the nine clusters are equally concentrated to within a factor of ≈1.2.

Cluster ID	$\frac{\int_0^{600''} T(\theta)\mathrm{d}\theta}{\int_0^{\theta_{500}} T(\theta)\mathrm{d}\theta}$
P014	17.3
P086	17.1
P097	17.8
P109	13.5
P170	36.0
P187	20.8
P190	19.4
P205	40.5
P351	45.07

in the legend by decreasing CARMA-8 Y_{500}, from Table 3, although in some cases, the differences are small. We would expect clusters with the most negative ΔT_0 values, the shallowest profiles and the largest θ_{500} to yield the largest Y_{500} values. While there is reasonable correspondence throughout our cluster sample, two clusters P351 and P187 are outliers in this relation. Computing $\int T(\theta)4\pi\theta^2\mathrm{d}\theta$ for each cluster from 0 to its θ_{500}, determined from model I (Table 3) shows that P351 (P187) has the highest (fifth highest) volume-integrated brightness temperature profile but only the fifth highest (second highest) Y_{500}.

In Fig. 3, right, we plot the upper and lower limits of the brightness temperature profiles allowed by the profile uncertainties for three clusters, P014, P109 and P205, chosen to span a wide range of profile shapes. It can be seen that the cluster candidates display a range of brightness temperature profiles that can be differentiated despite the uncertainties. In Table 10, by computing the ratio of the integral of the brightness temperature profile within (a) the 100-GHz *Planck* beam and (b) θ_{500} from Table 3, we quantify how concentrated each brightness temperature profile is. The profile concentration factors have a spread of a factor of ≈2.5, but, for six clusters, they agree within a factor of ≈1.2. Furthermore, the derived ellipticities shown in Tables 9 and 3, that can be constrained by the angular resolution of the CARMA-8 data, show significant evidence of morphological irregularity suggesting that these clusters may be disturbed and heterogeneous systems.

3 CLUSTER PARAMETER CONSTRAINTS FROM *Planck*

We used the public *Planck* PR1 all-sky maps to derive Y_{500} and θ_{500} values for our cluster candidates (Table 11). The values were derived using a multifrequency matched filter (Melin, Bartlett & Delabrouille 2006; Melin et al. 2012). The y profile from equation (4) is integrated over the cluster profile and then convolved with the *Planck* beam at the corresponding frequency; the matched filter leverages only the *Planck* high-frequency instrument data between 100 and 857 GHz because it has been seen that the large beams at lower frequencies result in dilution of the temperature decrement due to the cluster. The beam-integrated, frequency-dependent SZ signal is then fit with the scaled matched filter profile from equation (2) to derive Y_{500}; this process is repeated for the full range of parameters that we derive from the CARMA-8 data alone. The uncertainty in the derived Y_{500} is thus due to both the uncertainty in the cluster size (Planck Collaboration XXIX 2014b) which, in turn, factors in all the other dependencies as described earlier, as well as the signal to noise of the temperature decrement in the *Planck* data. The large beam of *Planck*, FWHM ≈ 10 arcmin at 100 GHz, makes it challenging to constrain the cluster size unless the clusters are at low redshift and thereby significantly extended. For this reason, Planck Collaboration XXIX (2014b) provided the full range of Y_{500}–θ_{500} contours which are consistent with the *Planck* data.

For the comparison here, there are two *Planck*-derived Y_{500} estimates; Y_{500} was calculated using the cluster position and size

Table 11. Y_{500} and θ_{500} values derived from the release 1 *Planck* all-sky maps. The second and third columns contain Y_{500} and θ_{500} from a blind analysis of the *Planck* maps, that is, from an analysis of *Planck* data alone, without any constraints from ancillary data. The fourth column contains the *Planck* Y_{500} values calculated at the CARMA-8 cluster centroids using the CARMA-8-derived θ_{500} measurements. The ratio of Y_{500} values from columns 2 and 4 is given in the fifth column, while the ratio of θ_{500} from the blind *Planck* (column 2) and the CARMA-8 analyses is provided in column 6 (where the CARMA-8 θ_{500} values have been taken from Table 3.

Cluster ID	Y_{500} blind (arcmin^2 $\times10^{-4}$)	θ_{500} blind (arcmin)	Y_{500} (arcmin^2 $\times10^{-4}$)	$Y_{500,\mathrm{blind}}/Y_{500}$	$\Theta_{500,\mathrm{blind}}/\theta_{500}$
P014	13.2 ± 6.4	4.23	$8.2^{+1.9}_{-1.8}$	1.61	0.98
P086	6.9 ± 2.5	4.23	$5.8^{+1.9}_{-1.7}$	1.18	1.14
P097	3.8 ± 0.8	0.92	$3.1^{+0.6}_{-0.5}$	1.22	0.29
P109	5.4 ± 1.2	0.92	$5.9^{+1.5}_{-1.1}$	0.91	0.30
P170	11.7 ± 4.1	4.75	$7.1^{+2.0}_{-1.2}$	1.65	1.76
P187	11.5 ± 4.1	3.35	$10.5^{+3.7}_{-3.4}$	1.10	0.82
P190	7.9 ± 4.7	4.75	$5.9^{+1.9}_{-1.7}$	1.33	1.36
P205	10.3 ± 4.9	3.35	$10.7^{+3.9}_{-3.8}$	0.97	0.68
P351	14.2 ± 9.7	6.75	$8.9^{+2.9}_{-3.1}$	1.60	1.27

(θ_{500}) obtained from the higher resolution CARMA-8 data, while $Y_{500,\mathrm{blind}}$ was computed using the *Planck* data alone without using the CARMA-8 size constraints. Similarly, $\theta_{500,\,\mathrm{blind}}$ is a measure of the angular size of the cluster using exclusively the *Planck* data; this value is weakly constrained and, thus, no cluster-specific errors are given for this parameter in Table 11. At this point, it is important to note that the quoted uncertainty for $Y_{500,\,\mathrm{blind}}$ is an underestimate; the quoted error for this parameter is based on the spread in Y_{500} at the best-fitting $\theta_{500,\,\mathrm{blind}}$ and is proportional to the signal to noise of the cluster in the *Planck* data i.e, without considering the error on $\theta_{500,\,blind}$ which is very large. However, the uncertainty in Y_{500} is accurate since it propagates the true uncertainty in θ_{500} from the CARMA-8 data into the estimation of this quantity from the *Planck* maps.

The uncertainty in $Y_{500,\,\mathrm{blind}}$ from using the CARMA-8 size measurement has gone down by ≈60 per cent on average, despite the fact that the $Y_{500,\,\mathrm{blind}}$ does not include the uncertainty resulting from the unknown cluster size. If the true uncertainty in $Y_{500,\,\mathrm{blind}}$ had been taken into account, the uncertainty would have gone down by more than an order of magnitude after application of the CARMA-8-derived cluster-size constraints. The mean ratio of $Y_{500,\,\mathrm{blind}}$ to Y_{500} is 1.3 and, in fact, Y_{500} is only larger than its blind counterpart for two systems. Differences in the profile shapes account for $Y_{500,\,\mathrm{blind}}$ being larger than Y_{500} for three systems, P014, P097 and P187, for which $\theta_{500,\,\mathrm{blind}}$ is smaller than θ_{500} measured by CARMA-8.

4 IMPROVED CONSTRAINTS ON Y_{500} AND θ_{500} FROM THE USE OF A *Planck* PRIOR ON Y_{500} IN THE ANALYSIS OF CARMA-8 DATA

Due to their higher resolution (a factor of $\gtrsim$5), the CARMA-8 data are better suited than the *Planck* data to constrain θ_{500}. On the other hand, the large *Planck* beam (FWHM ≈10 arcmin at 100 GHz) allows the sampling parameter Y_{T} for our clusters (all of which have $\theta_{500} \lesssim 5$ arcmin) to be measured directly, which is not the case for the CARMA-8 data due to its finite sampling of the *uv* plane and the missing zero-spacing information (a feature of all interferometers). We have exploited this complementarity of the *Planck* and CARMA-8 data to reduce uncertainties in Y_{500} and θ_{500}. In order to do this, we filtered out the parameter chains (henceforth chains) for the analysis of the CARMA-8 data (model I) that had values of Y_{500} outside the range allowed by the *Planck* $Y_{500} \pm 1\sigma$ results (Table 11). We refer to the results from the remaining set of chains as the joint results (Table 12). This may seem like circular logic, in that we have used CARMA-8 unbiased parameter constraints to fit the *Planck* data and then using the range of derived *Planck* Y_{500} values, which would otherwise span an order of magnitude wider range, to constrain the CARMA-8 parameter chains. In an ideal world, we would have fit both data sets jointly at the same time; however, the software to handle CARMA-8 and *Planck* data together simultaneously does not exist and with the closure of CARMA, will not be ever developed.

In Fig. 4, we plot the 2D marginalized distributions for Y_{500} and θ_{500} for the CARMA-8 data alone (black contours) and for the joint results (magenta contours). Similar approaches comparing *Planck* data with higher resolution SZ data have been undertaken by Planck Collaboration II (2013a) (with AMI), Muchovej et al. (2012) (with CARMA), Sayers et al. (2013a) (with BOLOCAM) and Perrott et al. (2015) (with AMI). Clearly, the introduction of cluster-size constraints from high-resolution interferometry data provides a powerful way to shrink the uncertainties in Y_{500}–θ_{500} phase space.

Table 12. Columns 2 and 3 contain the joint θ_{500} and Y_{500} values, which were computed by truncating the output of the CARMA-8 chains to have Y_{500} values in the range allowed by the *Planck* results (column 4 in Table 11).

Cluster ID	$\Theta_{500,\mathrm{Joint}}$ (arcmin)	$Y_{500,\mathrm{Joint}}$ (arcmin^2 $\times10^{-4}$)
P014	$3.8^{+0.1}_{-0.3}$	$8.2^{+0.6}_{-0.7}$
P086	$2.7^{+0.3}_{-0.4}$	$5.5^{+0.5}_{-0.7}$
P097	$2.1^{+0.1}_{-0.3}$	$3.3^{+0.2}_{-0.2}$
P109	$3.2^{+0.2}_{-0.4}$	$5.7^{+0.3}_{-0.5}$
P170	$3.3^{+0.2}_{-0.2}$	$7.1^{+0.4}_{-0.6}$
P187	$4.2^{+0.3}_{-0.4}$	$10^{+1.0}_{-1.4}$
P190	$2.8^{+0.2}_{-0.2}$	$5.8^{+0.5}_{-0.7}$
P205	$4.3^{+0.3}_{-0.5}$	$10^{+1.1}_{-1.5}$
P351	$5.5^{+0.2}_{-0.8}$	$8^{+0.7}_{-1.2}$

5 ESTIMATION OF RADIO-SOURCE CONTAMINATION IN THE *Planck* 143-GHZ DATA

In order to assess if there are any cluster-specific offsets in the *Planck* Y_{500} values, we estimate the percentage of radio-source contamination to the *Planck* SZ decrement at 143 GHz – an important *Planck* frequency band for cluster identification – from the 1.4-GHz NVSS catalogue of radio sources. Spectral indices between 1.4 and 31 GHz were calculated in table 3 in Paper I for sources detected in both our CARMA-8 LB data and in NVSS, giving a mean value of α_{s} of 0.72. We use this value for α_{s} to predict the source-flux densities at 100 and 143 GHz of all NVSS sources within 5 arcmin of the CARMA-8 pointing centre, following the same relation as we did earlier, $S_\nu \propto \nu^{-\alpha_{\mathrm{s}}}$.

The accuracy of the derived 100- and 143-GHz source fluxes is uncertain. First, there is source variability due to the fact the NVSS and CARMA-8 data were not taken simultaneously, which could affect the 1.4–31 GHz spectral index. Secondly, we assume the spectral index between 1.4 and 31 GHz is the same as for 1.4–143 GHz, which need not be true. Thirdly, we deduce α_{s} from a small number of sources, all of which must be bright in the LB data and apply this α_{s} to lower flux sources found in the deeper NVSS data, for which α_{s} might be different. However, previous work shows that this value for α_{s} is not unreasonable. Comparison of 31-GHz data with 1.4-GHz data on field sources has been previously done by Muchovej et al. (2010) and Mason et al. (2009). For the former, the 1.4–31 GHz spectral-index distribution peaked at 0.7, while, for the latter, it had a mean value of 0.7. The Muchovej et al. study also investigated the spectral index distribution between 5 and 31 GHz and located its peak at ≈0.8. Radio-source properties in cluster fields have been characterized in e.g. Coble et al. (2007) tend to have a steep spectrum. In particular, the 1.4–31 GHz spectral index for the Coble et al. study had a mean value of 0.72. Sayers et al. (2013a) explored the 1.4–31 GHz radio source spectral properties towards 45 massive cluster systems and obtained a median value for α_{s} of 0.89, which they showed was consistent with the 30–140 GHz spectral indices. The radio-source population used to estimate the contamination to the *Planck* 143 GHz signal is likely to be a combination of field and cluster-bound radio sources due to the size of the *Planck* beam and the fact that some of the candidates might be spurious *Planck* detections. Overall, given the differences

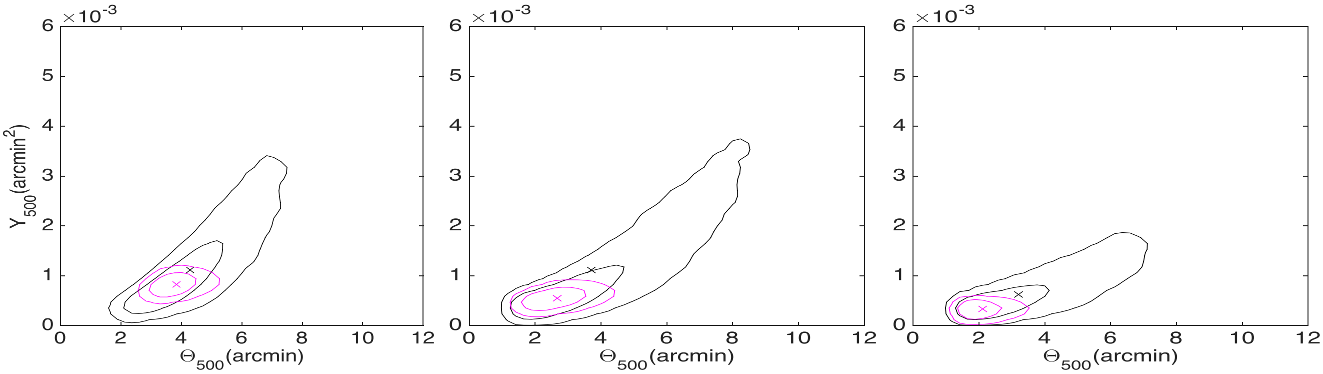

(a) Left to right: P014, P086, P097

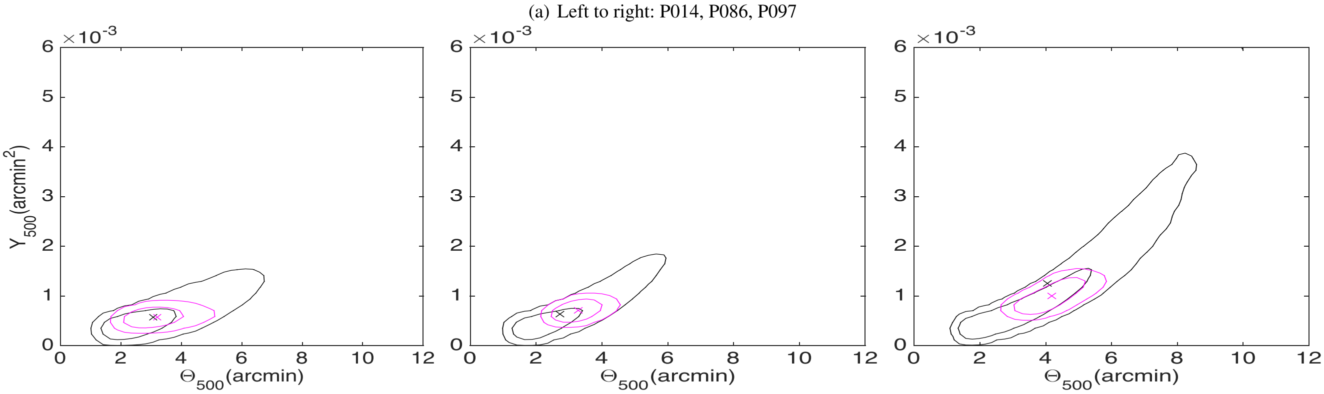

(b) Left to right: P109, P170, P187

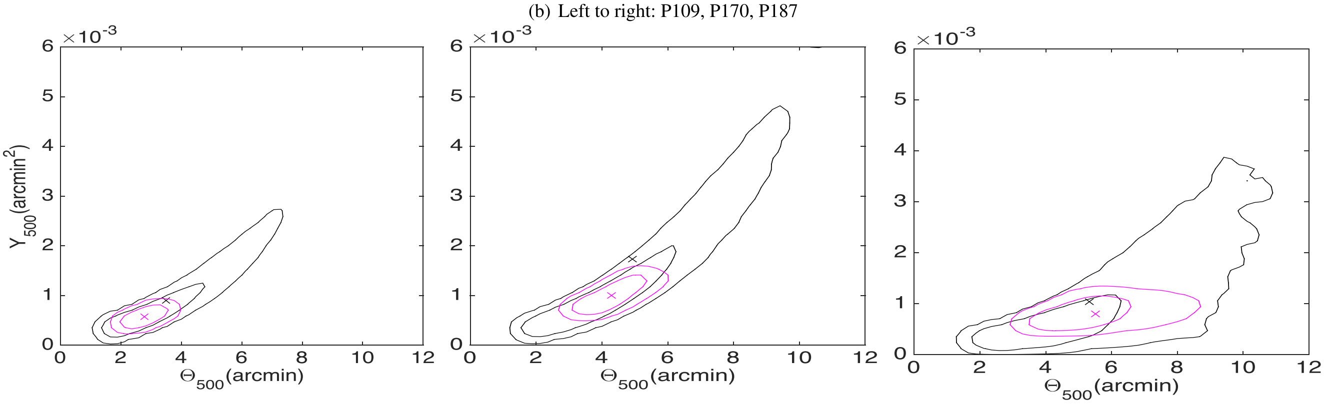

(c) Left to right: P190, P205, P351

Figure 4. 2D posterior distributions in the Y_{500}–θ_{500} plane for the CARMA-8 data alone in black contours and for the CARMA-8 data using a *Planck* prior on Y_{500} (column 4 in Table 11), in magenta contours, to which we refer to as the joint CARMA-*Planck* constraints. The *y*-axis is Y_{500} in units of arcmin^2 and the *x*-axis is θ_{500} in units of arcmin. The lower and upper limits of the *y*-axis are 0 and 0.006 arcmin^2, labelled in steps of 0.001 arcmin^2 and for the *x*-axis, they are 0–12 arcmin, labelled in steps of 2 arcmin. The inner and outer contours in each set indicate the areas enclosing the 68 per cent and 95 per cent of the probability distribution. For all the candidate clusters, there is a dramatic improvement in Y_{500}–θ_{500} uncertainties when the CARMA and *Planck* data are jointly analysed to yield cluster parameters.

in the source selection and in frequency, and the agreement with other studies, our choice of $\alpha_s = 0.72$ seems to be a reasonable one.

In Table 13, we list the sum of all the predicted radio-source-flux densities at 100 and 143 GHz of all the NVSS-detected sources within 5 arcmin of our pointing centre. This yields an approximate measure of the radio-source contamination in the *Planck* beam at these frequencies. The mean of the sum of all integrated source-flux densities at 1.4 GHz is 61.0 mJy (standard deviation, sd 71.6); at 100 GHz it is 2.8 mJy (sd = 3.3) and at 143 GHz, it is 2.2 mJy (sd = 2.6). The SZ decrement towards each cluster candidate within the 143 GHz *Planck* beam is given in Table 13, together with the (expected) percentage of radio-source contamination to the *Planck* cluster signal at this frequency, which, on average, amounts to ≈2.9 per cent. The mean percentage contamination to the *Planck* SZ decrement would drop to ≈1.3 per cent if we used the Sayers et al. (2013a) $\alpha_s = 0.89$ and would increase to ≈5 per cent if we used a flatter α_s of 0.6. Thus, we expect the flux density from unresolved radio sources towards our cluster candidates to be an insignificant contribution to the *Planck* SZ flux, although individual clusters may have radio-source contamination at the ∼5–15 per cent level.

Table 13. Estimated radio-source contamination in *Planck* for clusters in our sample. Column 2 provides the sum of all the 1.4-GHz 'deconvolved' integrated flux–density measurements of NVSS sources detected within 5 arcmin of the *Planck* cluster centroid. Assuming a spectral index, α_s, of 0.72 (see Paper I for details), we extrapolated the NVSS flux densities to find the total flux density at 100 and 143 GHz (columns 3 and 4), the most relevant *Planck* bands for SZ. The fifth column contains the (candidate) SZ decrement measured in the *Planck* 143-GHz band within its beam area in mJy. The last column presents the percentage radio-source contamination to the 143-GHz *Planck* candidate SZ decrement. This percentage is likely to be the amount by which the SZ flux is underestimated in the *Planck* data, since these are faint sources below the *Planck* point source detection limit.

Cluster ID	Σ Flux densities at 1.4 GHz	Σ Flux densities at 100 GHz	Σ Flux densities at 143 GHz	143-GHz *Planck* SZ decrement inside beam	per cent radio-source contamination to *Planck* SZ
P014	131.20	6.10	4.70	−77.3	6.1
P028	120.70	5.60	4.40	−90.2	4.9
P031	14.10	0.60	0.50	−57.6	0.9
P049	62.60	2.90	2.30	−55.7	4.1
P052	293.00	13.60	10.50	−67.6	15.5
P057	126.80	6.00	4.60	−96.5	4.8
P090	4.30	0.20	0.20	−42.0	0.5
P097	5.90	0.20	0.20	−38.4	0.5
P109	54.90	2.60	2.00	−108.4	1.8
P121	31.30	1.50	1.10	−79.9	1.4
P134	15.80	0.70	0.60	−54.9	1.1
P138	37.00	1.70	1.30	−66.8	1.9
P170	18.40	0.90	0.70	−141.1	0.5
P187	71.10	3.40	2.60	−70.4	3.7
P190	18.90	0.80	0.70	−48.6	1.4
P205	15.80	0.70	0.60	−82.1	0.7
P264	8.40	0.40	0.30	−61.1	0.5
P351	67.10	3.10	2.40	−101.7	2.4

6 DISCUSSION

6.1 Use of priors

When undertaking a Bayesian analysis, it is important not only to check that the priors on individual parameters are sufficiently wide, such that the distributions are not being truncated, but also that the effective prior is not biasing the cluster parameter results. Here, the term effective prior refers to the prior that is being placed on a model parameter while taking into account the combined effect from all the priors given to the set of sampling parameters. What may seem to be inconspicuous priors on individual parameters can occasionally jointly re-shape the high dimensional parameter space in unphysical ways; this was noticed in e.g. Zwart et al. (2011). Biases from effective priors should be investigated by undertaking the analysis without data, i.e. by setting the likelihood function to a constant value. Such studies for the models used in this work have been presented in AMI Consortium: Rodríguez-Gonzálvez et al. (2012) and Olamaie et al. (2013) and have determined that the combination of all the model priors does not bias the results.

6.2 Cluster position and morphology

The mean separation (and standard deviation, sd) of the CARMA-8 centroids from model I and the *Planck* position is ≈1.5 arcmin (0.5); see Tables 3 and 9 for offsets from the CARMA-8 SZ decrement to the *Planck* position. This offset is comparable to the offsets between *Planck* and X-ray cluster centroids found for the Early Sunyaev Zel'dovich (Planck Collaboration VIII 2011b) and the Planck Sunyaev Zel'dovich (PSZ) datasets (Planck Collaboration XXIX 2014b), which were typically ≈2 arcmin and 70 arcsec, respectively. The cluster candidate with the largest separation, ≈2.5 arcmin, is P014. The high-resolution CARMA-8 data allow for the reduction of positional uncertainties in the *Planck* catalogue for candidate clusters from a few arcminutes to within ≲30 arcsec. This is crucial, amongst other things, for the efficient follow-up of these candidate systems at other wavelengths. P351 has the largest positional uncertainties for both parameterizations (≈40 arcsec), a likely indication of a poorer fit of the models to the data; since the noise in the CARMA-8 data is one of the smallest of the sample, the system is detected at 5.6σ in the SB data and the source environment is quite benign with a single detected LB radio point source 4 arcmin from the pointing centre with a flux of 3.3 mJy, which was could be subtracted well (see Paper I for further details). Interestingly, this cluster stands out in the β parametrization for having the shallowest profile (Fig. 3), and in the gNFW parametrization for having the largest θ_{500}. Overall, the positional uncertainties from the shape-fitting model I, tends to be larger than that from the radial profile based model II, typically by a factor of 1.2 and reaching a factor of 2.8. The different parameter degeneracies resulting from each analysis is likely to be the dominant cause for this. As shown in fig. 1 of AMI Consortium: Rodríguez-Gonzálvez et al. (2012), in the Y_{500}–θ_{500} plane, the 2D marginalized distribution for the cluster size is significantly narrower for the β parametrization (model II) than for the gNFW parametrization (model I).

On average, cluster candidates with CARMA-8 detections have θ_s and θ_{500} in the ranges of 2–5 and 2.7–5.3 arcsec, respectively, with typical uncertainties of 1.5 arcmin (see Table 3). We note that these are not independent parameters but related by $\theta_{500} \approx \theta_s \times 1.2$. The largest cluster has $\theta_s = 5$ arcmin, $\theta_{500} = 5.3$ arcmin (P351) and the smallest $\theta_s = 2$ arcmin, $\theta_{500} = 2.7$ arcmin (P170). In Paper I, we estimated the photometric redshifts for our cluster candidates with a CARMA-8 SZ detection and found that on average, they appeared to be at $z \approx 0.5$; we also have tentative spectroscopic

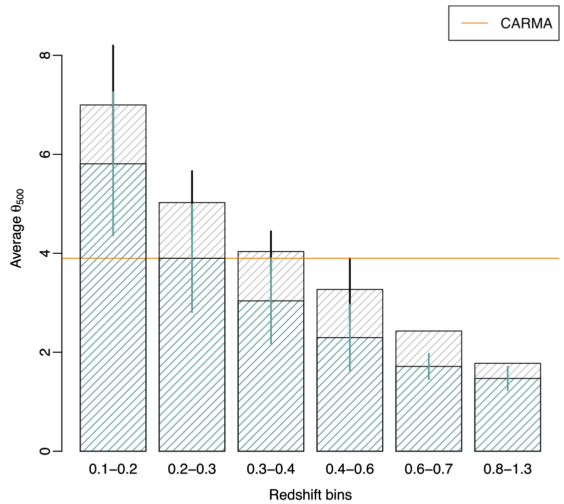

Figure 5. Average θ_{500} in arcmin, $\langle\theta_{500}\rangle$, values calculated from the MCXC catalogue (Piffaretti et al. 2011) within a series of redshift bins, as indicated in the x-axis, e.g. the first bin represents $\langle\theta_{500}\rangle$ for MCXC clusters with $0.1 \le z < 0.2$. The bar plots filled with blue diagonal lines use all the relevant MCXC cluster entries to get $\langle\theta_{500}\rangle$, while those filled with grey diagonal lines only include the more massive clusters, $M_{500} > 4 \times 10^{14}\,\mathrm{M}_{\odot}$, which we expect to be more representative of our target sample as *Planck* detects the most massive clusters. Standard deviations are displayed as vertical lines. The average CARMA-8-derived θ_{500} estimate for our clusters is depicted with an orange horizontal line. This plot suggests the typical θ_{500} values for our clusters are most comparable with the θ_{500} values for MCXC clusters at $0.2 \lesssim z \lesssim 0.4$. Furthermore, when combined with our photometric redshift measurements in Paper I which place our clusters at $z \sim 0.5$, the data suggest that we are finding the largest, most massive clusters at intermediate redshifts.

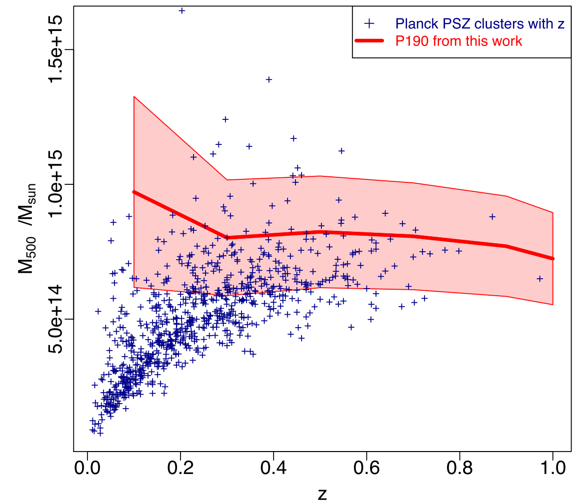

Figure 6. M_{500} estimates for candidate cluster P190 as a function of redshift. To obtain the M_{500} measurements a third parametrization, model III (Section 6.3; Olamaie et al. 2013), which samples directly from the cluster mass, was implemented in the McAdam analysis. Since this model requires redshift information as an input, but spectroscopic-redshift information is not available for most of our candidate clusters, we ran this model run six times, from $z = 0.1$ to 1.0 in steps of 0.2. The range of M_{500} values encompassing 68 per cent of the probability distribution is shown in the red shaded area. We overplot the M_{500} estimates from the *Planck* PSZ cluster catalogue (Planck Collaboration XXIX 2014b) for entries with an associated redshift in blue + signs. The PSZ catalogue of clusters contains the majority of the most massive X-ray-detected clusters in the MCXC catalogue. Hence, the clusters in our sample, which have SZ signatures similar to that of P190, are amongst the most massive known systems at intermediate redshifts.

identification of a galaxy that is part of P097 at $z = 0.565$. The relatively small values for θ_{500} would support the notion that our systems are at intermediate redshifts ($z \gtrsim 0.5$). In comparison, for the Meta-Catalogue of X-Ray detected Clusters of galaxies (MCXC) catalogue of X-ray-identified clusters (Piffaretti et al. 2011), whose mean redshift is 0.18, the mean X-ray-derived θ_{500} is a factor of 2 larger. In Fig. 5, we plot the average θ_{500} within a series of redshift ranges starting from $z = 0.1$ for all MCXC clusters (in blue) and for only the more massive, $M_{500} > 4 \times 10^{14}\,\mathrm{M}_{\odot}$, clusters (in grey), which should be more representative of the cluster candidates analysed here (see Fig. 6) and mark the average CARMA-8-derived θ_{500} for our clusters with an orange line. This plot suggests that the θ_{500} values for our clusters are most comparable with the θ_{500} values for MCXC clusters at $0.2 \lesssim z \lesssim 0.4$.

The resolution of the CARMA-8 data, together with the often poor SNRs and complications in the analysis, e.g. regarding the presence radio sources towards some systems, makes getting the accurate measurements of the ellipticity η challenging, with typical uncertainties in η of 0.2 (Table 3). These uncertainties are fairly large, yet the use of a spherical model is physically motivated and allows the propagation of realistic sources of uncertainty. Moreover, comparison of models with spherical and elliptical geometries for similar data from AMI is presented in AMI Consortium: Hurley-Walker et al. (2012) which show the Bayesian evidences are too alike for model comparison, indicating that the addition of complexity to the model by introducing an ellipticity parameter is not significantly penalized. In Perrott et al. (2015), modelling of AMI cluster data with and ellipsoidal GNFW profile instead of a spherical profile had a negligible effect on the constraints in Y. Our CARMA data with higher noise levels and generally more benign source environments should show even smaller effects.

η values close to 1 would be expected for relaxed systems, whose projected signal is close to spheroidal, unless the main merger axis is along the line of sight. On the other hand, disturbed clusters should have $\eta \to 0.5$. Some evidence for a correlation of cluster ellipticity and dynamical state has been found in simulations, e.g, Krause et al. (2012) and data, e.g. Kolokotronis et al. (2001) (X-ray), Plionis (2002) (X-ray and optical) and AMI Consortium: Rodríguez-Gonzálvez et al. (2012) (SZ), although this correlation has a large scatter. Hence, from the derived fits to the data, we conclude that at least a minority of clusters in our sample is likely to be comprised by large, dynamically active systems, unlikely to have fully virialized, which is not surprising given the intermediate redshifts of the sample.

6.3 Cluster-mass estimate

To estimate the total cluster mass M_{500} within r_{500}, we use the Olamaie et al. (2013) cluster parametrization, which samples directly from M_{200}.[6] This model describes the cluster dark matter halo with an NFW profile (Navarro et al. 1996) and the pressure profile with a gNFW profile (Nagai et al. 2007b), using the set

[6] M_{500} is determined by calculating r_{500}, which, in turn, is computed by equating the expression for mass from the NFW density profile within r_{500} and the mass within an spherical volume of radius r_{500} under the assumption of spherical geometry. Under this NFW–gNFW-based cluster parametrization the relation between M_{200} and M_{500} is $M_{200} = 1.35 \times M_{500}$. For further information on this cluster model, see Olamaie et al. (2013).

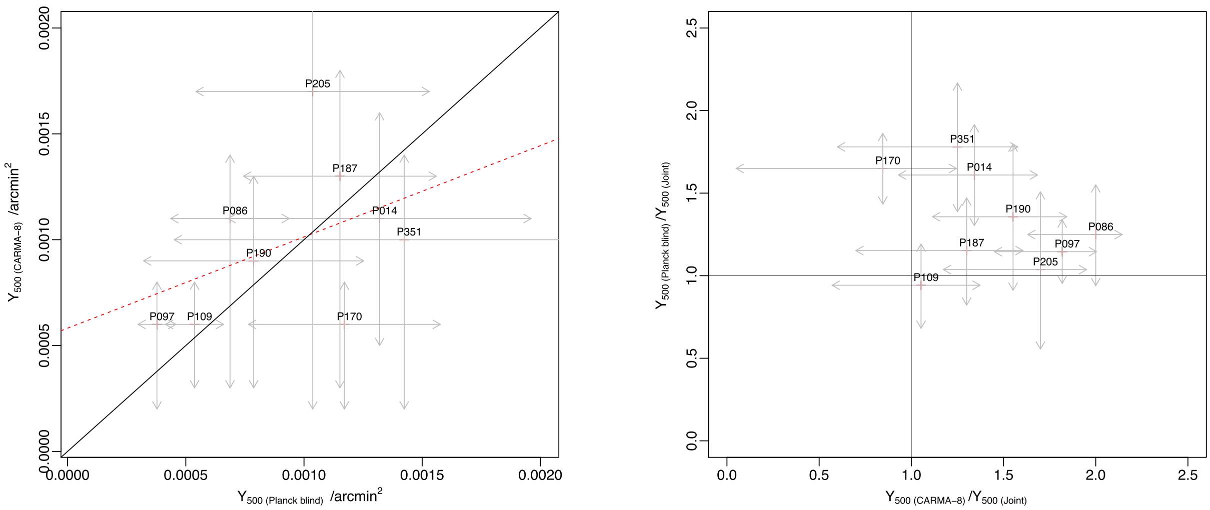

Figure 7. Left: Y_{500} measured by CARMA-8 against the blind *Planck* Y_{500}. No strong bias indications are detected between the *Planck*, blind and CARMA-8 Y_{500} results. The best-fitting (red, dotted) and 1:1 (black, solid) lines are included in this plot. Right: ratio of the *Planck*, blind Y_{500} and the joint Y_{500} values against the ratio of the CARMA-8 Y_{500} and the joint Y_{500}. For Y_{500}, both the CARMA-8 and *Planck*, blind values are practically always higher than the joint values by as much as a factor of 2.

of gNFW parameters derived by Arnaud et al. (2010). There are two other additional assumptions of this model: (1) the gas is in hydrostatic equilibrium and (2) the gas mass fraction is small compared to unity ($\lesssim$0.15).[7] The cluster redshift is a necessary input to this parametrization in the absence of spectroscopic data towards our cluster candidates, to get an accurate redshift estimate.[8] We obtained spectroscopic confirmation for P097, coarse photometric redshifts based on Sloan Digital Sky Survey (SDSS) and *WISE* colours were calculated in Paper I. In Fig. 6, we plot the M_{500} estimate (mean values are depicted by the thick line and the area covering the 68 per cent of the probability distribution has been shaded in red) as a function of z for one of our cluster candidates, P190. To produce this plot, we ran the Olamaie et al. (2013) cluster parametrization six times using a Delta-prior on redshift, which we set to values from 0.1 to 1.0 in steps of 0.2. We chose P190 since it is quite representative of our cluster candidates and, at 8σ, where σ is the SB rms, it has the best SNR of the sample (see table 2 in Paper I). The photometric-redshift estimate for P190 from Paper I was 0.5, which is also the average expected photometric redshift for the sample of CARMA-8 SZ detections. At this redshift, $M_{500} = 0.8 \pm 0.2 \times 10^{15}\,\mathrm{M}_{\odot}$. As seen in Fig. 6, after $z \approx 0.3$, M_{500} is a fairly flat function of z (since the z dependence in the model is carried by the angular diameter distance), such that, to one significant figure, our mean value is identical.

We have measured the spectroscopic redshift of a likely galaxy member of P097 through Keck/MOSFIRE *Y*-band spectroscopy. We deem it a likely member, given that it is situated close to the peak of the CARMA SZ decrement (within the 4σ contour) and close to a group of tightly clustered galaxies. We calculated M_{500} for this cluster, as we did for P190 in the previous section, setting the redshift prior to a delta function at $z = 0.565$ and obtained $M_{500} = 0.7 \pm 0.2 \times 10^{15}\,\mathrm{M}_{\odot}$, supporting the notion that our sample of clusters are some of the most massive clusters at $z \gtrsim 0.5$. Further follow-up of this sample in the X-rays and through weak lensing measurements with *Euclid* will help constrain the mass of these clusters more strongly.

6.4 The Y_{500}–θ_{500} degeneracy

In Fig. 4, the 2D marginalized posterior distributions in the Y_{500}–θ_{500} plane for (i) the CARMA-8 data alone and (ii) the joint analysis of CARMA-8 and *Planck* data are displayed for each cluster candidate with an SZ detection in the CARMA-8 data. It is clear from these plots and from Table 11 that there is good overlap between the *Planck* and CARMA-8-derived cluster parameter space for all of the candidate clusters. The range of *Planck* Y_{500} values after application of the θ_{500} priors from CARMA-8 are within the 68 per cent contours for the CARMA-only analysis. While the *Planck*-only range of $Y_{500,\,blind}$ values is wide, in combination with the θ_{500} constraints from the higher resolution CARMA-8 data, the Y_{500}–θ_{500} space is significantly reduced. To explore this further, in Fig. 7, we have plotted:

(i) the relation between Y_{500} from CARMA-8 and from the *Planck*, blind analysis $Y_{500,\,\mathrm{blind}}$ (left-hand panel),

(ii) the ratio of Y_{500} from the *Planck*, blind analysis and from the joint results against the ratio of Y_{500} from fits to CARMA-8 data and from the joint analysis (right-hand panel).

In Fig. 8, we present similar plots for θ_{500}. Inspection of Figs 7 and 8, left-hand panels, shows that the *Planck*, blind values for Y_{500}, as well as for θ_{500}, appear unbiased with respect to those from CARMA-8. As expected, due to *Planck*'s low angular resolution, the overall agreement between the *Planck*, blind measurements and those of CARMA-8 are much better for Y_{500} than for θ_{500}, with $\langle \Theta_{500,\,\mathrm{CARMA\text{-}8}}/\Theta_{500,\,\mathrm{Planck\ blind}} \rangle = 1.5$, sd $=$ 1.1 and $\left\langle Y_{500,\mathrm{CARMA-8}}/Y_{500,\mathrm{Planck\ blind}} \right\rangle = 1.1$, sd $= 0.4$. This good

[7] Extensive work has been done to characterize the hydrostatic mass bias, which has been shown to range between $\approx$5 and 45 per cent depending on dynamical state in numerical simulations (e.g. Rasia et al. 2006; Nagai, Vikhlinin & Kravtsov 2007a; Molnar et al. 2010) and studies comparing SZ and weak lensing mass estimates (e.g. Zhang et al. 2010; Mahdavi et al. 2013).

[8] P187 might be an exception as the observational evidence shows that it is likely to be associated with a well-known Abell cluster, Abell 586, at $z = 0.171$.

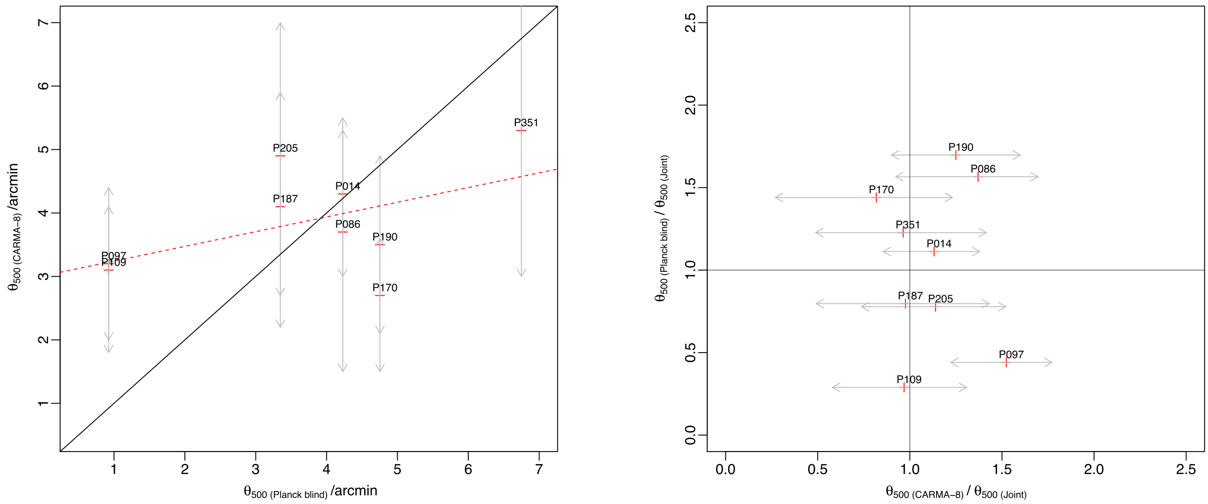

Figure 8. Left: θ_{500} measured by CARMA-8 against the blind *Planck* θ_{500}. Uncertainties on the *Planck*, blind θ_{500} are not included as they are determined by the large FWHM of the *Planck* beam and can range up to 10 arcmin. The best-fitting (red, dotted) and 1:1 (black, solid) lines are included in this plot. Right: ratio of the blind *Planck* θ_{500} and the joint θ_{500} against the ratio of the CARMA-8 θ_{500} and the joint θ_{500}. No strong systematic differences are seen between the different θ_{500} estimates. The higher resolution of the CARMA-8 data allows θ_{500} to be constrained much more strongly than using *Planck* data alone.

agreement in Y_{500} is interesting since recent results by Von der Linden et al. (2014) indicated that *Planck* masses are lower than the weak lensing masses typically by ≈30 per cent among a sample of 22 clusters selected differently to those studies here. Such a large correction to the masses would indeed alleviate the tension found in (Planck Collaboration XX 2013a), where the 95 per cent probability contours in the σ_8–$\Omega_{\rm m}$ plane derived from cluster data and from the CMB temperature power spectrum do not agree, when accounting for up to a 20 per cent bias from the assumption of hydrostatic equilibrium in the X-ray-based cluster-mass scaling relations. Since we find no signs of bias between the Y_{500} measurements from *Planck* and CARMA-8, this might indicate the bias arises when comparing masses rather than Y_{500}, that is, from the choice of scaling relations used to estimate the cluster mass. Although, our cluster sample is relatively small and our parameter uncertainties are substantial, other sources of bias in the SZ, X-ray and lensing measurements need to be investigated further with the same samples of objects rather than cluster samples selected in different ways and extending over different redshift ranges.

The right-hand panel of Fig. 7 shows that for all but two candidate clusters, the Y_{500} measurements derived from the joint analysis are consistently lower than from the independent analysis of the *Planck*, blind and CARMA-8 data sets, sometimes by as much as a factor of 2. The average magnitude and range of the shift from the independent-to-joint Y_{500} values are similar for the CARMA-8 and the *Planck*, blind analysis, with $\langle \frac{Y_{\rm 500,blind}}{Y_{\rm 500,Joint}} \rangle = 1.3$, sd = 0.3, $\langle \frac{Y_{\rm 500,CARMA-8}}{Y_{\rm 500,Joint}} \rangle = 1.4$, sd = 0.4. In the case of θ_{500}, Fig. 8 (right), there is no systematic offset between the joint results and those from either CARMA-8 or *Planck*, blind. On average, the agreement between the joint and independent results appears to be good, $\langle \frac{\Theta_{\rm 500,blind}}{\Theta_{\rm 500,Joint}} \rangle = 1.0$, sd = 0.5, $\langle \frac{\Theta_{\rm 500,CARMA-8}}{\Theta_{\rm 500,Joint}} \rangle = 1.1$, sd = 0.2, but, in the case of the *Planck*, blind measurements, the large standard deviations are an indication of its poor resolution.

We have quantified the improvements in the constraints for Y_{500} and θ_{500} derived from the independent analyses of *Planck* and CARMA-8 data with respect to the joint results. The largest improvement is seen for θ_{500} *Planck* blind, as this parameter is only weakly constrained by *Planck* data alone, with an associated uncertainty anywhere up to ≈10 arcmin. Yet, the advantage of a joint *Planck* and CARMA-8 analysis is very significant, for both θ_{500} and Y_{500} and for both the CARMA-8 and *Planck* results, with uncertainties dropping by $\gtrsim$400 per cent. We find improvements in the SNR of Y_{500} measurements to be of a factor of ≈5 (≈4) between the *Planck*, blind measurements and the joint values; the first factor corresponds to the lower bound 68 per cent errors and the second to the upper bound. Similarly, these improvements were of ≈76 (≈37) between the *Planck*, blind measurements and the joint values for SNRs for θ_{500}. As mentioned in Section 4, the SZ measurements from *Planck* and CARMA-8 data are complementary as they probe different cluster scales at different resolutions. Moreover, since the Y_{500}–θ_{500} degeneracy for each data set have different orientations (an effect already reported in Planck Collaboration II 2013a), a joint analysis looking at the overlapping regions will result in a further reduction of parameter space.

6.5 Comparison with the AMI-*Planck* study

The AMI (Zwart et al. 2008) has followed up ≈100 *Planck*-detected systems, most of which are previously confirmed systems. Comparison of AMI and *Planck* results for 11 clusters in Planck Collaboration II (2013a) showed that as seen by *Planck*, clusters appear larger and brighter than by AMI. This result has now been confirmed in a larger upcoming study (Perrott et al. 2015). In Fig. 9, we compare AMI and CARMA-8 values for Y_{500} against the *Planck* results. We note that the analysis pipeline for the processing of CARMA-8 data in this work is identical to that of AMI, allowing for a clean comparison between both studies.

All 11 clusters in the AMI-Planck study are known X-ray clusters (except for two) and are at $0.11 < z < 0.55$, with an average z of 0.3 and a mean θ_{500} of 4.8. Our sample of cluster candidates is expected to have a mean (coarse) photometric redshift of ≈0.5 (see Paper I) and a mean θ_{500} of 3.9. The smaller angular extent of our sample of objects could be indicative that they are, in fact, at higher redshifts. As pointed out in Planck Collaboration II (2013a), the Y_{500} measurements from *Planck* are systematically

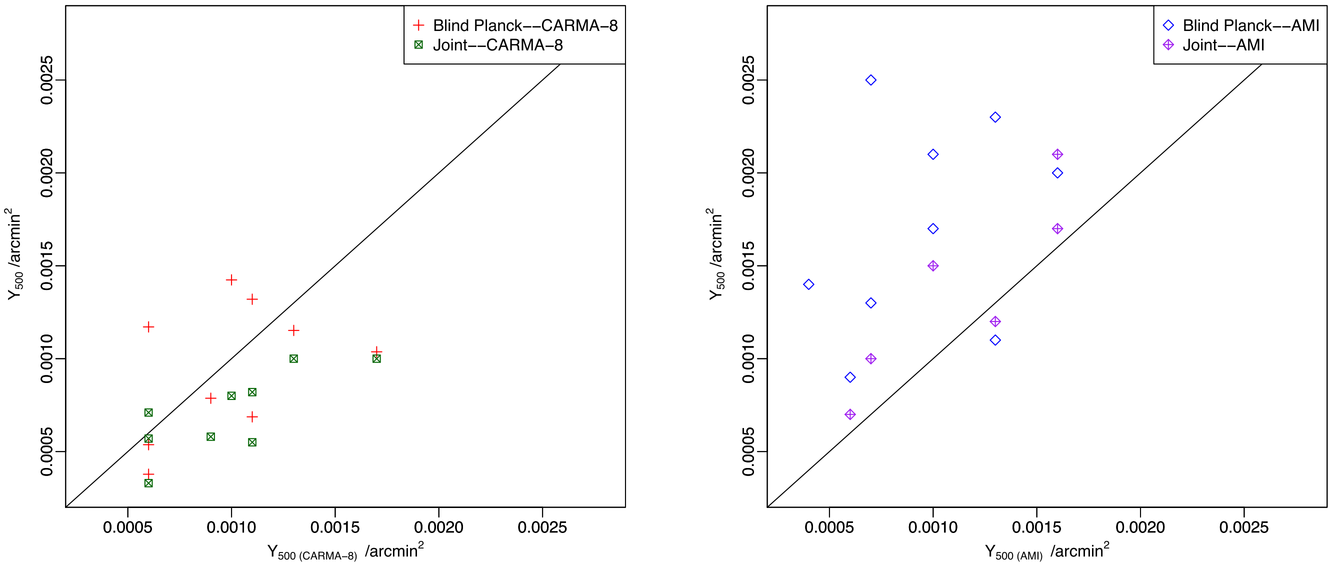

Figure 9. Left: plot of Y_{500} derived from two different analyses of *Planck* data against Y_{500} derived from CARMA-8 data. We plot two sets of Y_{500} based on *Planck* measurements (i) using *Planck* data alone; these data points are referred to as 'blind' and are shown in red crosses and (ii) using the range of Y_{500} *Planck* (blind) values to constrain further the Y_{500} values obtained in the analysis of CARMA-8 data; these are referred to as 'joint' values and are shown in green crosses inside a square. In addition, we plot a 1 : 1 line in solid black. For the joint Y_{500} values, these are plotted on the y-axis, whilst keeping the x-axis as the CARMA-8 Y_{500} values. Right: plot of Y_{500} from several analyses of *Planck* data against Y_{500} from AMI. We plot two sets of Y_{500} based on *Planck* measurements: (i) using *Planck* data alone; these data points are referred to as 'blind' and are shown in blue diamonds and (ii) using the range of Y_{500} *Planck* (blind) values as a prior in the analysis of the AMI data; these are referred to as 'joint' values and are shown in purple + signs inside a diamond. For the joint Y_{500} values, these are plotted on the y-axis, whilst keeping the x-axis as the AMI Y_{500} values. In addition, we plot a 1: 1 line in solid black. Comparison of the left-hand and right-hand plots shows that the *Planck* (blind) measurements are generally in good agreement with CARMA-8, with no signs of systematic offsets between the two measurements. Calculating the *Planck* Y_{500} using the CARMA-8 θ_{500} and position measurements decreases the *Planck* Y_{500} estimates, which become systematically slightly lower than the CARMA-8 estimates (Table 11). This systematic difference is enhanced for the joint Y_{500} values. For AMI, the *Planck* blind Y_{500} values appear to be consistently higher than the AMI values for all but one cluster. While this difference narrows for the joint AMI-*Planck* Y_{500} estimates, it is not resolved. Hence, the AMI Y_{500} estimates are generally higher than those for *Planck*, irrespective of the choice of *Planck*-derived Y_{500} while CARMA-8 Y_{500} values are in good agreement with the (blind) *Planck* results, yet are generally higher when priors are applied to the CARMA-8 or *Planck* data.

higher than those for AMI, $\langle Y_{500,\mathrm{AMI}}/Y_{500,\mathrm{blind\,Planck}}\rangle = 0.6$, sd = 0.3. For the CARMA-8 results, on the other hand, we find good agreement between the CARMA-8 and *Planck*-blind Y_{500} values, $\langle Y_{500,\mathrm{CARMA-8}}/Y_{500,\mathrm{blind\,Planck}}\rangle = 1.1$, sd = 0.4, with no systematic offset between the two measurements.

Planck Collaboration II (2013a) point to the use of a fixed gNFW profile as a likely source for systematic discrepancies between the AMI-*Planck* results and they plan to investigate changes to the results when a wider range of profiles are allowed in the fitting process. With relatively similar spatial coverage between the CARMA-8 and AMI interferometers, the impact of using a gNFW profile in the analysis of either data set should be comparable (for most cluster observations), though this will be investigated in detail in future work. The fact that despite this, the CARMA-8 measurements are in good agreement with *Planck* could mean that either the CARMA-8 and *Planck* data are both biased-high due to systematics yet to be determined, or the AMI data are biased low, or a combination of both of these options. We stress that the analysis pipeline for deriving cluster parameters in this work and in Planck Collaboration II (2013a) is the same. Apart from the (typically) relatively small changes in the *uv* sampling of both instruments, the major difference between the two data sets is that the radio-source contamination at 16 GHz tends to be much stronger than at 31 GHz, since radio sources in this frequency range tend to have steep falling spectra and, hence, it tends to have a smaller impact on the CARMA-8 data. That said, AMI has a separate array of antennas designed to make a simultaneous, sensitive, high-resolution map of the radio-source environment towards the cluster, in order to be able to detect and accurately model contaminating radio sources, even those with small flux densities (≈350 μJy beam^{-1}).

A more likely alternative is the intrinsic heterogeneity in the different cluster samples. At low redshifts, when a cluster is compact relative to the AMI beam, heterogeneities in the cluster profiles get averaged out and the cluster-integrated Y_{500} values agree with those from *Planck*. However, if the cluster is spatially extended relative to the beam, a fraction of the SZ flux is missed and that results in an underestimate of the AMI SZ flux relative to the *Planck* flux. Since our sample is at higher redshifts and appears to be less extended compared to the clusters presented in Planck Collaboration II (2013a), it is likely that profile heterogeneities are averaged out alleviating this effect seen in the low-z clusters. The prediction therefore is that more distant, compact clusters that are followed up by AMI will show better agreement in Y_{500} values with *Planck*, although hints of a size-dependence to the agreement are already seen in Planck Collaboration II (2013a).

The results from this comparison between *Planck*, AMI and CARMA-8 SZ measurements draw further attention to the need to understand the nature of systematics in the data, in order to use accurate cluster-mass estimates for cosmological studies. To address this, we plan to analyse a sample of clusters observed by all three instruments in the future.

7 CONCLUSIONS

We have undertaken high (1–2 arcmin) spatial resolution 31 GHz observations with CARMA-8 of 19 *Planck*-discovered cluster candidates associated with significant overdensities of galaxies in the *WISE* early data release ($\gtrsim$1 galaxies arcmin^{-2}). The data reduction, cluster validation and photometric-redshift estimation were presented in a previous article (Paper I). In this work, we used a Bayesian-analysis software package to analyse the CARMA-8 data. First, we used the Bayesian evidence to compare models with and without a cluster SZ signal in the CARMA-8 data to determine that nine clusters are robust SZ detections and two candidate clusters are most likely spurious. The data quality for the remaining targets was insufficient to confirm or rule out the presence of a cluster signal in the data.

Secondly, we analysed the nine CARMA-8 SZ detections with two cluster parameterizations. The first was based on a fixed-shape gNFW profile, following the model used in the analysis of *Planck* data (e.g. Planck Collaboration VIII 2011b), to facilitate a comparative study. The second was based on a β gas density profile that allows for the shape parameters to be fit. There is reasonable correspondence for the cluster characteristics derived from either parametrization, though there are some exceptions. In particular, we find that the volume-integrated brightness temperature within θ_{500} calculated using results from the β profile does not correlate well with Y_{500} from the gNFW parametrization for two systems. This suggests that differences in the adopted profile can have a significant impact on the cluster-parameter constraints derived from CARMA-8 data. Indeed, radial brightness temperature profiles for individual clusters obtained using the β model results exhibit a level of heterogeneity distinguishable outside the uncertainty, with the degree of concentration for the profiles within θ_{500} and within 600 arcsec ($\approx$ the FWHM of the 100-GHz *Planck* beam) being between $\approx$1 and 2.5 times different.

Cluster-parameter constraints from the gNFW parametrization showed that on average, the CARMA-8 SZ centroid is displaced from that of *Planck* by $\approx$1.5 arcmin. Overall, we find that our systems have relatively small θ_{500} estimates, with a mean value of 3.9 arcmin. This is a factor of 2 smaller than for the MCXC clusters, whose mean redshift is 0.18. This provides further, tentative, evidence to support the photometric-redshift estimates from Paper I, which expected the sample to have a mean z of $\approx$0.5. Using Keck/Multi-Object Spectrometer for Infra-Red Exploration (MOSFIRE) Y-band spectroscopy, we were able to confirm the redshift of a likely galaxy member of one of our cluster candidates, P097, to be at $z = 0.565$.

We analysed data towards P190, a representative candidate cluster for the sample, with a cluster parametrization that samples from the cluster mass. This parametrization requires z as an input. We ran it from a z of 0.1–1 in steps of 0.2. Beyond the $z > 0.3$ regime, the dependence of mass on z is very mild (with the mass remaining unchanged to within one significant figure). Our estimate for M_{500} at the expected average z of our sample, 0.5 (Paper I), is $0.8 \pm 0.2 \times 10^{15}$ M$_{\odot}$.

We compared the *Planck* (blind) and CARMA-8 measurements for Y_{500} and θ_{500}. Both sets of results appear to be unbiased and in excellent agreement, with $\langle Y_{500,\mathrm{CARMA-8}}/Y_{500,\mathrm{blind,Planck}}\rangle = 1.1$, sd = 0.4. and $\langle \Theta_{500,\mathrm{CARMA-8}}/\Theta_{500,\mathrm{blind,Planck}}\rangle = 1.5$, sd = 1.1, whose larger difference is a result of the poor spatial resolution of *Planck*. This is in contrast with the results from a similar study between AMI and *Planck* that reported systematic differences between these parameters for the two instruments, with *Planck* characterizing the clusters as larger (typically by $\approx$20 per cent) and brighter (by $\approx$35 per cent on average) than AMI. However, it should be emphasized that the clusters studied in this paper are, on average, at higher redshift and more compact than those in the AMI-*Planck* joint analysis.

Recent results by Von der Linden et al. (2014) find *Planck* masses to be biased low by $\approx$30 per cent with respect to weak lensing masses. This is similar to that suggested in Planck Collaboration XX (2013a) who consider the possibility of *Planck* masses to be biased low by 20–40 per cent to explain inconsistencies in their results from cluster data and the CMB temperature power spectrum. The good agreement between *Planck* and CARMA-8 Y_{500} measurements presented here, in contrast with the large differences in the *Planck* masses derived from X-ray-based scaling relations, could be an indication that the origin of the discrepancy lies primarily in the choice of scalings and in the heterogeneity in cluster profiles with increasing redshift. However, our sample size is small and our uncertainties substantial. A large multifrequency study of clusters, which included *Planck* and a high-resolution SZ experiment, like CARMA-8 or AMI, to check for systematics in Y_{500}, as well as lensing and X-ray data to investigate differences in cluster-mass estimates, would be beneficial to fully address this.

We exploited the complementarity of the *Planck* and CARMA-8 data sets – the former measures the entire cluster flux directly unlike the latter, which can, on the other hand, constrain θ_{500} – to reduce the size of the Y_{500}–θ_{500} degeneracy by applying a *Planck* prior on the Y_{500} obtained from CARMA-8 alone. We show how this joint analysis reduces uncertainties in Y_{500} derived from the *Planck* and CARMA-8 data individually by more than a factor of $\gtrsim$5.

In this article and in its companion paper (Paper I), we have demonstrated (1) an interesting technique for the selection of massive clusters at intermediate $z \gtrsim 0.5$ redshifts by cross-correlating *Planck* data with *WISE* and other data (2) a powerful method for breaking degeneracies in the Y_{500}(flux)–θ_{500}(size) plane and thus greatly improving constraints in these parameters.

ACKNOWLEDGEMENTS

We thank the anonymous referee for a careful reading of the manuscript and would also like to acknowledge helpful discussions with Y. Perrott and A. Lasenby. We thank the staff of the Owens Valley Radio observatory and CARMA for their outstanding support; in particular, we would like to thank John Carpenter. Support for CARMA construction was derived from the Gordon and Betty Moore Foundation, the Kenneth T. and Eileen L. Norris Foundation, the James S. McDonnell Foundation, the Associates of the California Institute of Technology, the University of Chicago, the states of California, Illinois, and Maryland, and the National Science Foundation. CARMA development and operations were supported by the National Science Foundation under a cooperative agreement, and by the CARMA partner universities. The *Planck* results used in this study are based on observations obtained with the *Planck* satellite (http://www.esa.int/Planck), an ESA science mission with instruments and contributions directly funded by ESA Member States, NASA, and Canada. We are very grateful to the AMI Collaboration for allowing us to use their software and analysis techniques in this work and for useful discussions. A small amount of the data presented herein were obtained at the W.M. Keck Observatory, which is operated as a scientific partnership among the California Institute of Technology, the University of California and the National Aeronautics and Space Administration. The Observatory was made possible by the generous financial support of the W.M. Keck Foundation.

REFERENCES

Allen S. W., Evrard A. E., Mantz A. B., 2011, ARA&A, 49, 409
Arnaud M., Pratt G. W., Piffaretti R., Böhringer H., Croston J. H., Pointecouteau E., 2010, A&A, 517, A92
Atrio-Barandela F., Kashlinsky A., Kocevski D., Ebeling H., 2008, ApJ, 675, L57
Carvalho P., Rocha G., Hobson M. P., Lasenby A., 2012, A&A, 70, 677
Cavaliere A., Fusco-Femiano R., 1978, MNRAS, 427, 1384
Coble K. et al., 2007, AJ, 134, 897
Czakon N. G. et al., 2015, ApJ, 806, 18
Feroz F., Hobson M P., 2008, MNRAS 400, 984
Feroz F., Hobson M. P., Bridges M., 2008, MNRAS 398, 1601
Feroz F. et al., 2009, MNRAS, 398, 2049
Fixsen D. J., Cheng E. S., Gales J. M., Mather J. C., Shafer R. A., Wright E. L., 1996, ApJ, 473, 576
Gettings D. P. et al., 2012, ApJ, 759, L23
Hinshaw G. et al., 2009, ApJS, 180, 225
Hurley-Walker N. et al.; AMI Consortium, 2012, MNRAS, 419, 2921
Itoh N., Kohyama Y., Nozawa S., 1998, ApJ, 502, 7
Jeffreys H., 1961. The Theory of Probability, 3rd edn. Oxford. Clarendon Press, Oxford
Jenkins C. R., Peacock J. A., 2011, MNRAS, 413, 2895
Jenkins C. R. et al., 2001, MNRAS, 321, 372
Kolokotronis V., Basilakos S., Plionis M., Georgantopoulos I., 2001, MNRAS, 320, 49
Krause E., Pierpaoli E., Dolag K., Borgani S., 2012, MNRAS, 419, 1766
Mahdavi A., Hoekstra H., Babul A., Bildfell C., Jeltema T., Henry J. P., 2013, ApJ, 767, 116
Mantz A. B. et al., 2014, ApJ, 794, 157
Marshall P. J., Hobson M. P., Slosar A., 2003, MNRAS, 346, 489
Mason B. S., Weintraub L., Sievers J., Bond J. R., Myers S. T., Pearson T. J., Readhead A. C. S., Shepherd M. C., 2009, ApJ, 704, 1433
Melin J.-B., Bartlett J. G., Delabrouille J., 2006, A&A, 459, 341
Melin J.-B. et al., 2012, A&A, 548, A51
Molnar S. M., Chiu I.-N., Umetsu K., Chen P., Hearn N., Broadhurst T., Bryan G., Shang C., 2010, ApJ, 724, L1
Mroczkowski T., 2011, ApJ, 728, L35
Mroczkowski T. et al., 2009, ApJ, 694, 1034
Muchovej S. et al., 2007, AAS, 39, #143.04
Muchovej S. et al., 2010, ApJ, 716, 521
Muchovej S., Leitch E., Culverhouse T., Carpenter J., Sievers J., 2012, ApJ, 749, 46
Nagai D., Vikhlinin A., Kravtsov A. V., 2007a, ApJ, 655, 98
Nagai D., Kravtsov A. V., Vikhlinin A., 2007b, ApJ, 668, 1
Navarro J. F., Frenk C. S., White S. D. M., 1996, ApJ, 462, 563
Olamaie M., Hobson M. P., Grainge K. J. B., 2013, MNRAS, 430, 1344
Olamaie M. et al.; AMI Consortium, 2012, MNRAS, 421, 1136
Papovich C., 2008, ApJ, 676, 206
Perrott Y. C. et al., 2015, A&A, 580, A95
Piffaretti R., Arnaud M., Pratt G. W., Pointecouteau E., Melin J.-B., 2011, A&A, 534, A109
Plagge T. et al., 2010, ApJ, 716, 1118
Planck Collaboration I, 2011a, A&A, 536, A1
Planck Collaboration VIII, 2011b, A&A, 536, A8
Planck Collaboration II, 2013a, A&A, 550, A128
Planck Collaboration V, 2013b, A&A, 550, A131
Planck Collaboration XX, 2014a, A&A, 571, A20
Planck Collaboration XXIX, 2014b, A&A, 571, A29
Plionis M., 2002, ApJ, 572, L67
Rasia E. et al., 2006, MNRAS, 369, 2013
Rodríguez-Gonzálvez C., Muchovej S., Chary R. R., 2015, MNRAS, 447, 902 (Paper I)
Rodríguez-Gonzálvez C. et al.; AMI Consortium, 2011, MNRAS, 414, 3751
Rodríguez-Gonzálvez C. et al.; AMI Consortium, 2012, MNRAS, 425, 162
Sayers J. et al., 2013a, ApJ, 764, 152
Sayers J. et al., 2013b, ApJ, 768, 177
Schammel et al., 2012, MNRAS, 431, 900
Shepherd M. C., 1997, in Hunt G., Payne H. E., eds, ASP Conf. Ser. Vol. 125, Astronomical Data Analysis Software and Systems VI. Astron. Soc. Pac., San Francisco, p. 77
Shimwell T. W. et al.; AMI Consortium, 2013a, MNRAS, 433, 2036
Shimwell T. W. et al.; AMI Consortium, 2013b, MNRAS, 433, 2920
Sunyaev R. A., Zel'dovich Y. B., 1972, Comments Astrophys. Space Phys., 4, 173
Tauber J. A. et al., 2010, A&A, 520, A1
Vikhlinin A., Markevitch M., Murray S. S., Jones C., Forman W., Van Speybroeck L., 2005, ApJ, 628, 655
Voit G. M., 2005, Rev. Mod. Phys., 77, 207
von der Linden A. et al., 2014, MNRAS, 443, 1973
Wright E. L. et al., 2010, AJ, 140, 1868
Zhang Y.-Y. et al., 2010, ApJ, 711, 1033
Zwart J. T. L. et al., 2008, MNRAS, 391, 1545
Zwart J. T. L. et al., 2011, MNRAS, 418, 2754

This paper has been typeset from a TEX/LATEX file prepared by the author.